Chapter 10

Underground Tag Tests

All data will be presented in B-scan format to aide in the visualization of both tags and pipe. The raw data requires post-processing to be interpreted. These post-processing steps include cleaning up the data, applying gain to the B-scans and finally transforming the data. By eye, the tags will be more detectable, however functions can be applied for a more systematic approach to detect these automatically.

Starting with cleanup of the data, the first thing in this step is to shift the results with time zero correction in order. This moves the beginning of the B-scan to match with when the pulse is received from the ground. After that, a noise filter is applied to reduce the background noise to see object in the ground a bit clearer as noted in Fig. 10.1. This figure has an empty pipe with and without background removal along noting where the noise floor of these scans are with the green line at 40 ns or about 1.75 m, which is fairly typical for this frequency [13]. Gain then needs to applied to the B-scan in order to see objects that are deeper in the ground as much

as those closer to the surface due to the attenuation per meter of the soil, noted in Chapter 2. When applying the gain, there can be multiple points at which to have certain gains. What this means is that the gain can be decreased at the start of the sample and significantly increased later in the sample. In the following results, they are modified by three points starting with -20 dB at the start of the scan, 40 dB in the middle and 58 dB at the end of the scan. If there is spurious interference from cell phones or other wireless communication, data needs to be filtered with a bandpass filter, however noting that this can also distort the information available in the traces. Hyperbolas in the B-scan occur due to diffraction of electromagnetic waves [44, 43]. Typically, to make the hyperbolas look like a solid object, migration techniques like backprojection, Stolts/F-k, or Kirchhoff algorithms would be applied here [61]. Many times this is used for single targets with one hyperbola, however if there are multiple hyperbolas, that migration step may severely distort the other hyperbolas with slightly different surrounding dielectrics due to varying speeds in the soil, sometimes resulting in upside down hyperbolas with over-migration. If they are corrected too much, they can provide less information, therefore these results do not reflect migration changes.

10.0.1 Co-Polarized Tags

Two major items were noted for the co-polarized tags during the in-ground tests that were not seen in the free-space tests. First, in addition to the secondary pulse from the transmission line, ringing continues on for tens of nano-seconds. Second, the ringing frequency varies with transmission line length. The ringing itself is not

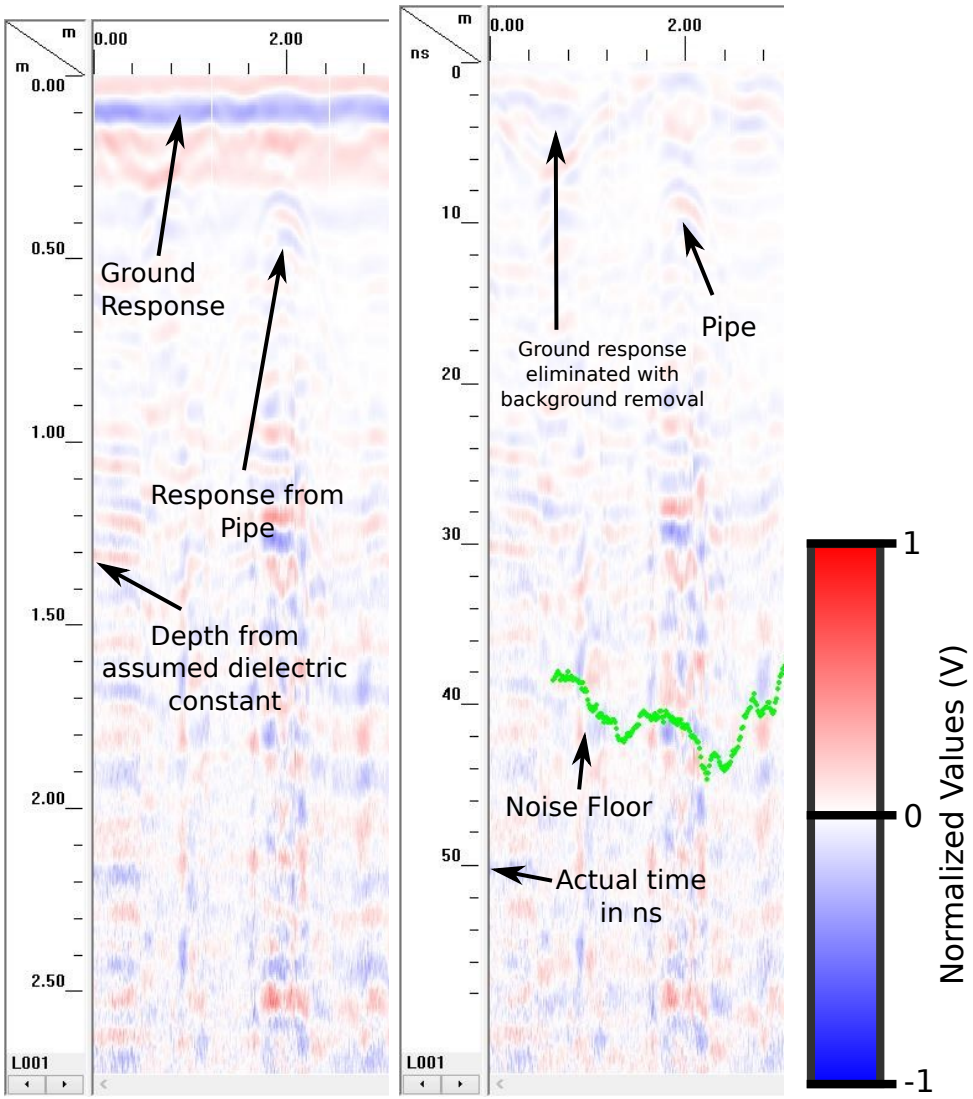

(a) (b) (c)

Figure 10.1: GPR B-scans for (a) empty pipe, (b) empty pipe with background removal and noise floor of scan on green line on 10 Jan 2018 and (c) GPR key. Note the green line is the estimated noise floor for each B-scan.

an artifact from the GPR, but is commonly seen in large open air voids or for that matter any transition that is not dispersive and has a lower dielectric constant [36].

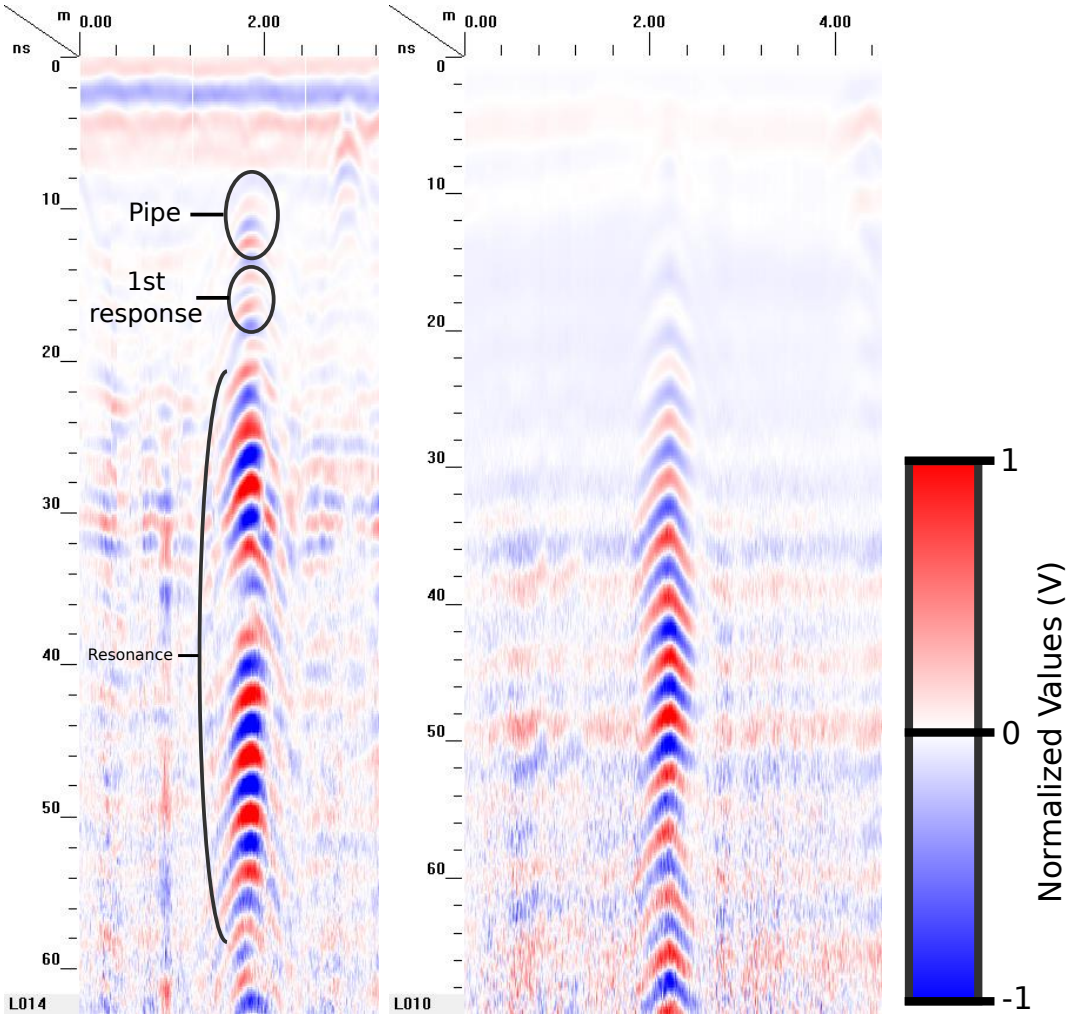

(a) (b) (c)

Figure 10.2: GPR B-scans for (a) short co-polarized tag at 400 MHz, (b) at 200 MHz and (c) GPR key.

For large voids, the pulse hits the top of the void and continues bouncing between the void boundaries. However, this occurs over and over again, if, for example, half of

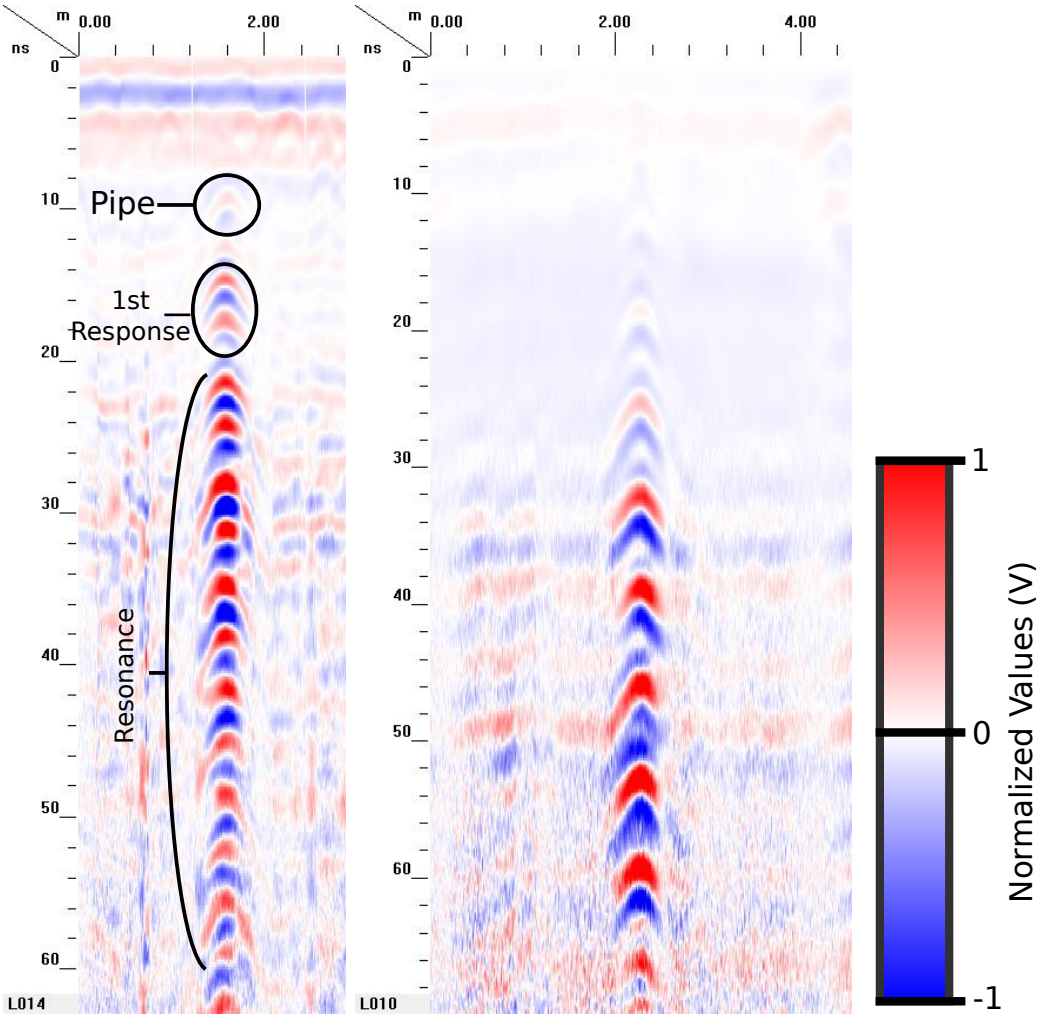

(a) (b) (c)

Figure 10.3: GPR B-scans for (a) long co-polarized tag at 400 MHz, (b) at 200 MHz and (c) GPR key.

the pulse's power is reflected and the other transmitted to the other side of the wall of the void. The GPR, with appropriate gain applied, continues to see these spikes over and over again for tens of ns after the initial reflection. Similar behavior has been observed with the tags, first the initial pulse hits the tag, then the pulse travels through the transmission line only hit either an open or short circuit, to go back and feed back into the antenna to produce the secondary pulse. In the case of the voids, the GPR might see many reverberations from a multi-path environment, where on the other hand these tags only produce a single path response. Since the antennas and transmission lines are not perfectly matched, see Table 6.2, it produces another reflection when the pulse goes into the feed line of the antenna. Both Fig. 10.2 and 10.3 display this effect. Normally these resonances are not ideal, since, in the perfect case, all the power would go from the transmission line into the antenna, but in this case it's quite beneficial, even if it horrifies many antenna designers. Likewise, if the free space tests would have used a power amplifier and a low noise amplifier, this effect may have been seen earlier.

The GPR sees that secondary pulse repeat at a specific frequency depending on how long the transmission line is. For the short transmission lines it repeats every 4 ns and for the long transmission lines it repeats every 7 ns. If this ringing continues on for say 50 ns, it is already outside of the noise floor of the surrounding soil where usable data cannot be extracted from anything else that might be deeper. By that, if the noise floor is at 25 ns and an object is 30 ns away, the GPR should not be able to see the object since it is under the noise. However tens of ns after the noise floor cuts off, the signal from the tag still rings over the noise even with its faint

responses. Fig. 10.4 compares the large difference with noise floor measurements between a B-scan with a tag in it and a B-scan without a tag in it. The B-scan without the tag has a consistent noise floor of around 1.4 m, however when a tag is inserted, the function to calculate the noise floor thinks there is a dip down to 2.25 m. Such jumps in the noise floor like this further reveal when the tag is present.

This response can be further detected if the FFT of each individual A-scan is taken, where that ringing translates into a single frequency in the time domain with the code in the first appendix where it takes a .csv input, which came from GP Workbench converting the file from the B-scan file into a .csv file, and outputs a FFT of the entire B-scan. Contrasting with the fairly empty and flat FFT response of an empty pipe in Fig. 10.5, FFTs, shown in Fig. 10.6 and 10.7 for short and long co-polarized tags respectively indicate that another data processing method can further reveal the location of the tag. Compared to this plotting method in Python, the RADAN software can do the same thing, however it normalizes the frequency response per each A-scan, limiting the usefulness of the conversion since the difference between each A-scan cannot be noted as much.

Note the heavy responses at 150, 300 and 450 MHz for the long co-polarized tags. All resonating tags also heavily change the phase response to the GPR such that it produces a constant phase along the frequency spectrum. The short delay tags seem to only have heavy frequency responses at 200 MHz. Both produce significant phase changes across the entire spectrum of the FFT. To further visualize these tags, the FFTs can be limited in amplitude with cutoff points.

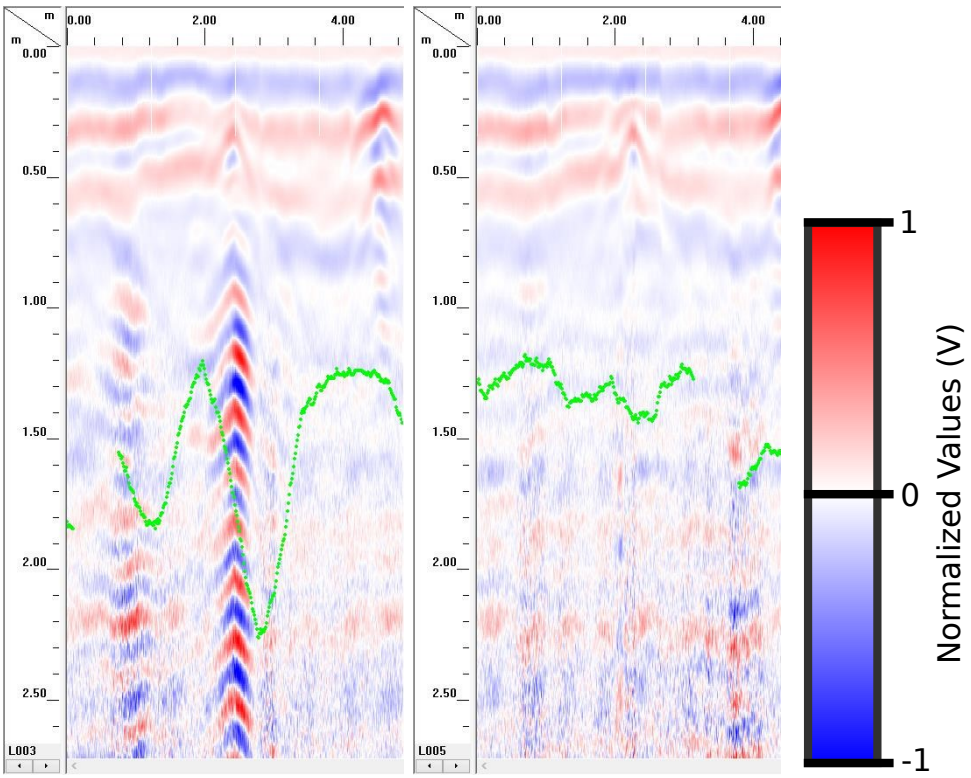

(a) (b) (c)

Figure 10.4: GPR B-scans with noise floor measurements for (a) long co-polarized tags, (b) pipe, and (c) GPR key. Note the green line is the estimated noise floor for each B-scan at 1.4 m.

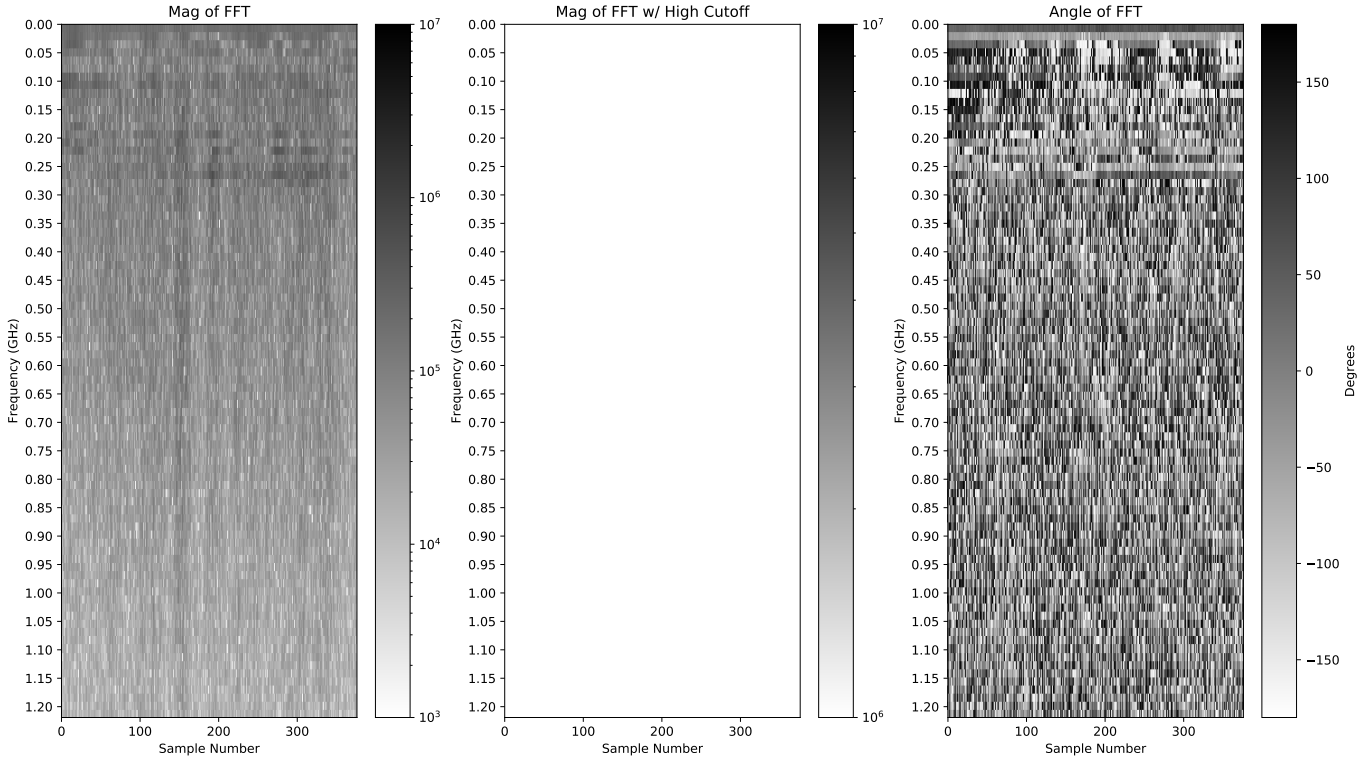

(a)

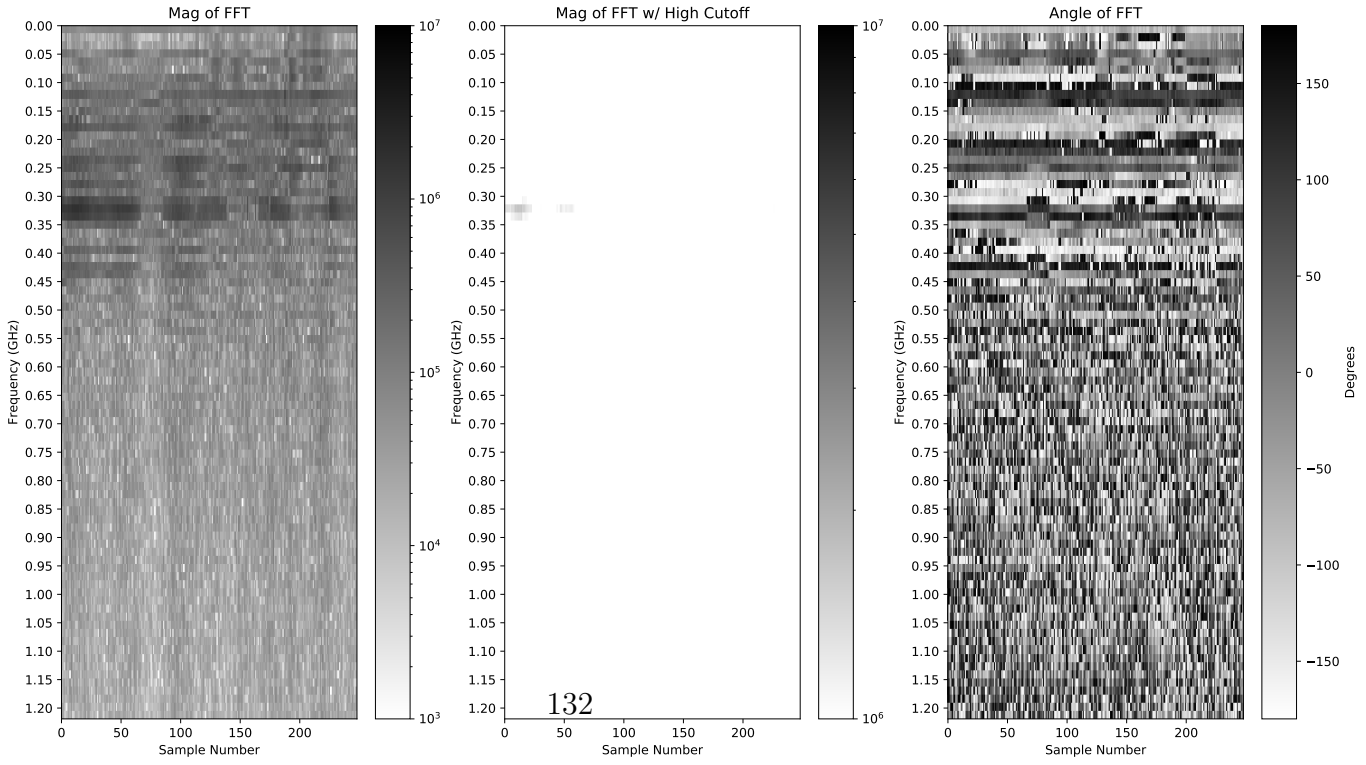

(b)

Figure 10.5: FFTs for an empty pipe at (a) 200 MHz and (b) 400 MHz.

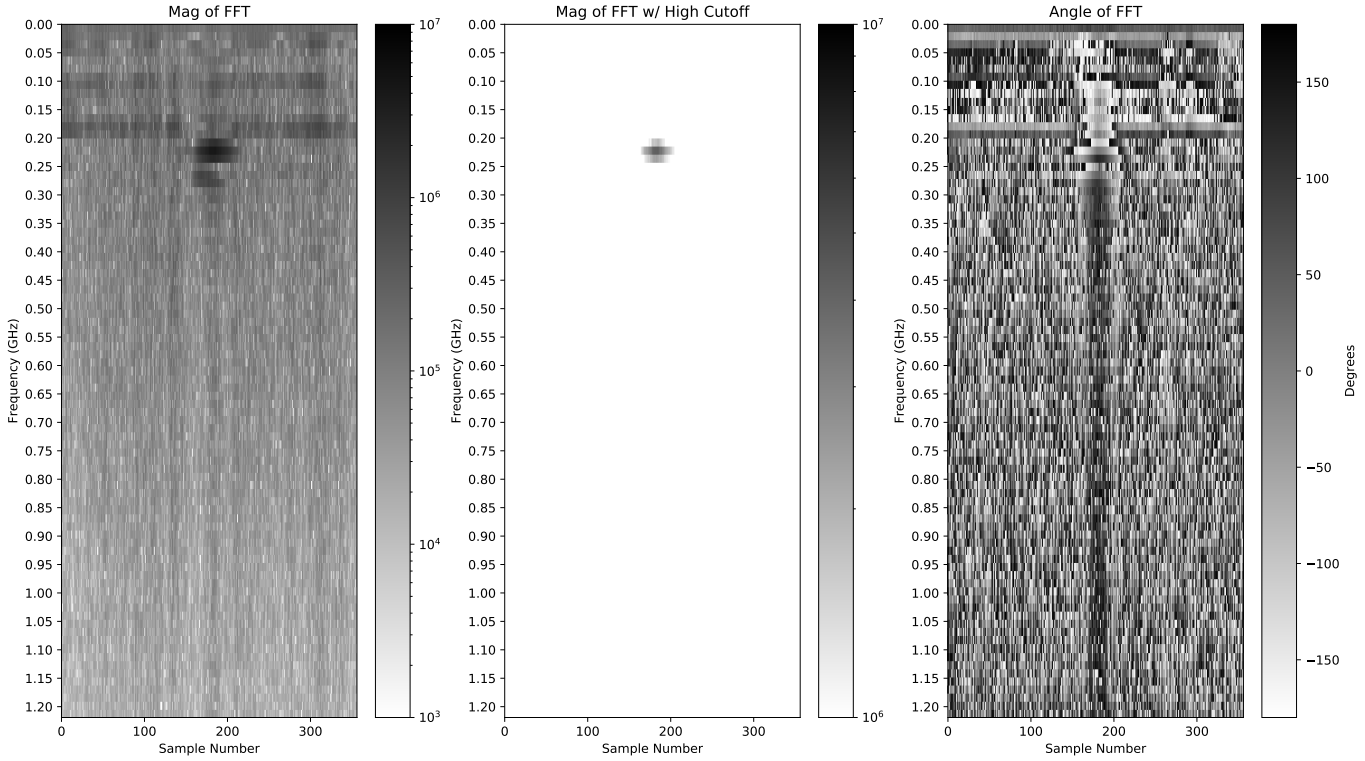

(a)

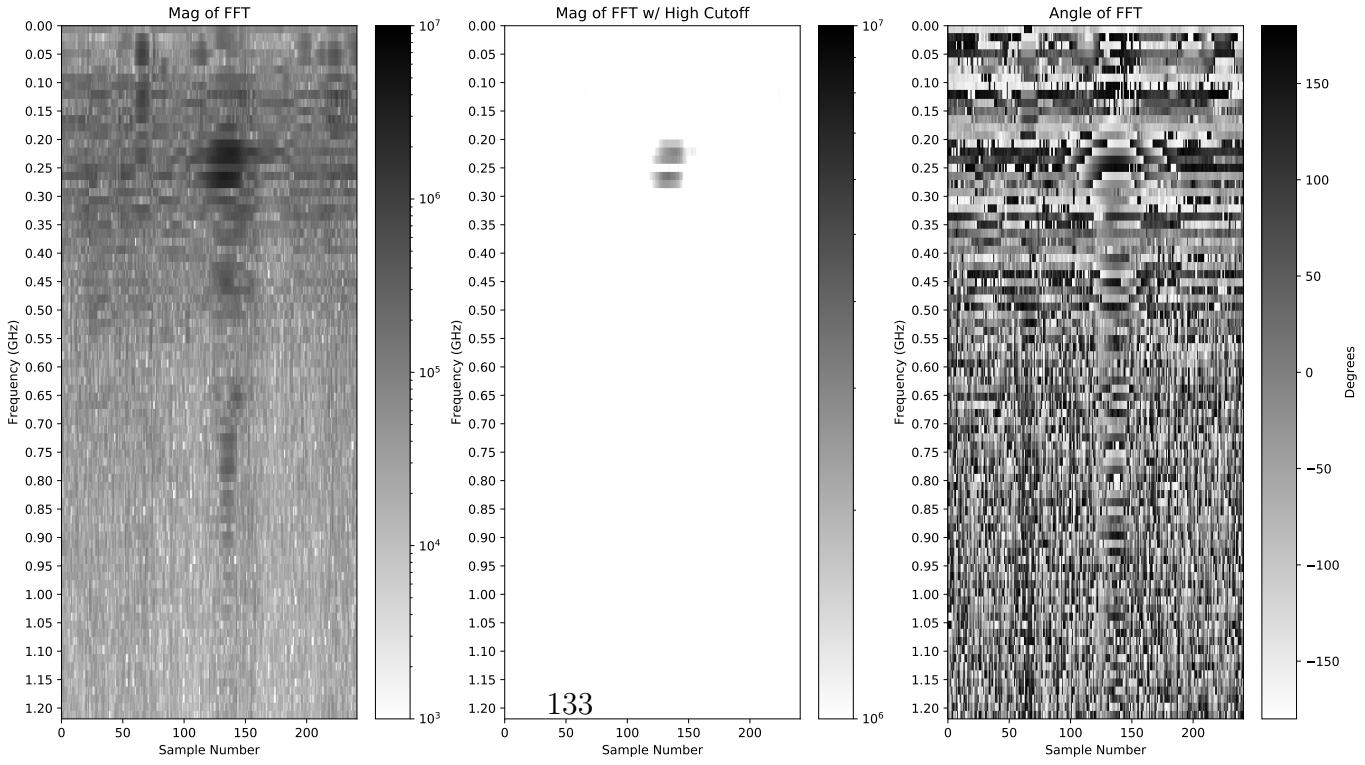

(b)

Figure 10.6: FFTs for short co-polarized tags at (a) 200 MHz and (b) 400 MHz.

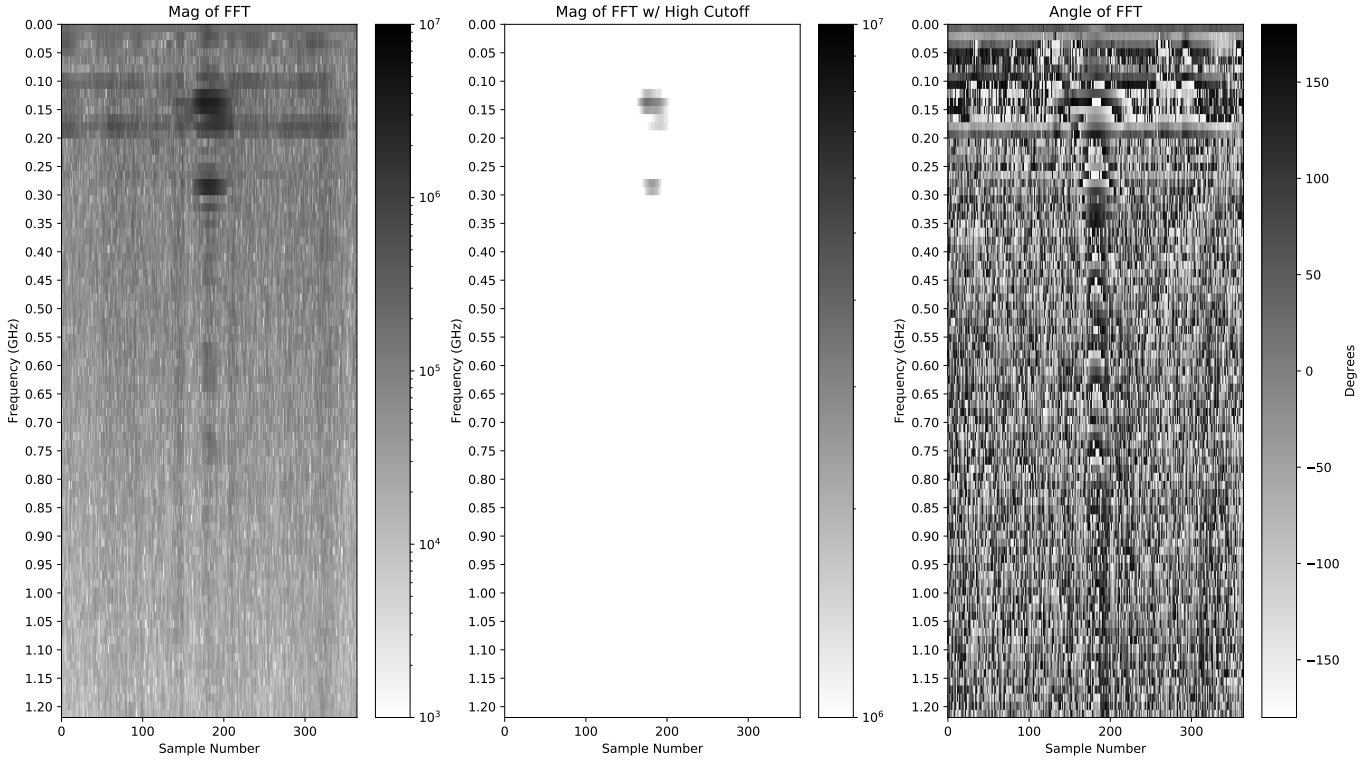

(a)

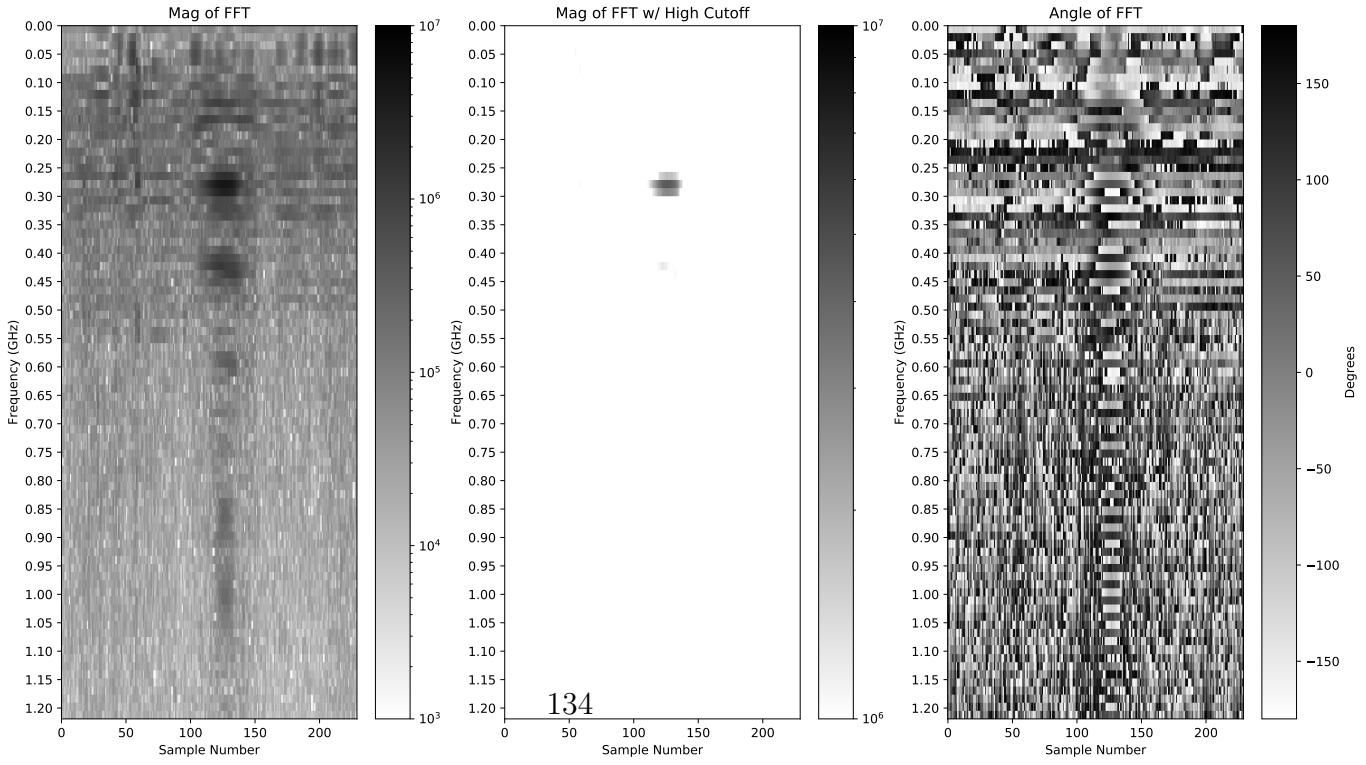

(b)

Figure 10.7: FFTs for long co-polarized tags at (a) 200 MHz and (b) 400 MHz.

10.0.2 Cross-Polarized Tags

One would imagine that even if the cross polarization tags have a polarization mismatch they still would, however these cross-polarized tags are too well matched. Take for example the double bowtie antenna, it matches to itself since they both have the same shape, interacts with the same materials and with no transmission line to speak of. This response is almost the same as the short cross polarized antenna since the length is less than a quarter wavelength of the center frequency which for 400 MHz is about 16 cm and for 200 MHz is about 33 cm. This lack of response is noted in both Fig. 10.9 and 10.10 when only the response from the pipe, as expected, is seen. However when the transmission line is longer, the ringing, seen previously in the co-polarized tags, every 5 ns as displayed in Fig. 10.8.

Fig. 10.11 indicates that the long CP tag has a similar response to the short co-polarized tag with a frequency response at 200 MHz. The long cross-polarization tag in these tests has a stronger response when in use with the 200 MHz GPR than the 400 MHz GPR. In the B-scan, the resonances can barely be seen at 400 MHz and consequentially do not have a large enough signal to overcome the noise when transferring into the frequency domain. However, there are stronger responses using the 200 MHz GPR, both seen in the B-scan and FFT of the tag. The bowtie and short cross polarized tags signatures again were masked by the pipe and were too well matched to each other to produce any resonating response.

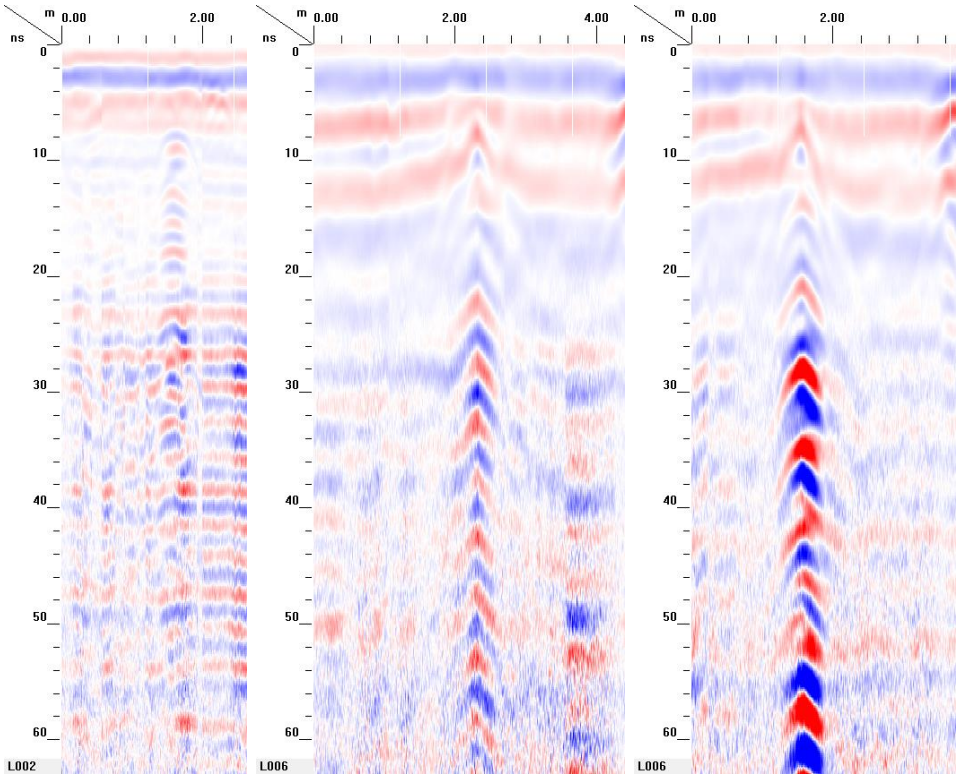

(a) (b) (c)

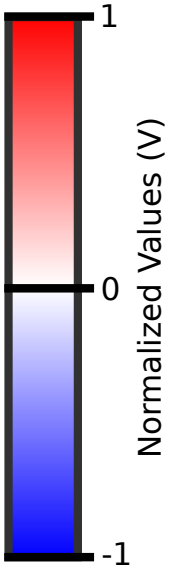

(d)

Figure 10.8: GPR B-scans for (a) long cross-polarized tag at 45° at 400 MHz, (b) at 200 MHz, (c) long co-polarized tag at 45° at 200 MHz for comparison and (d) GPR key.

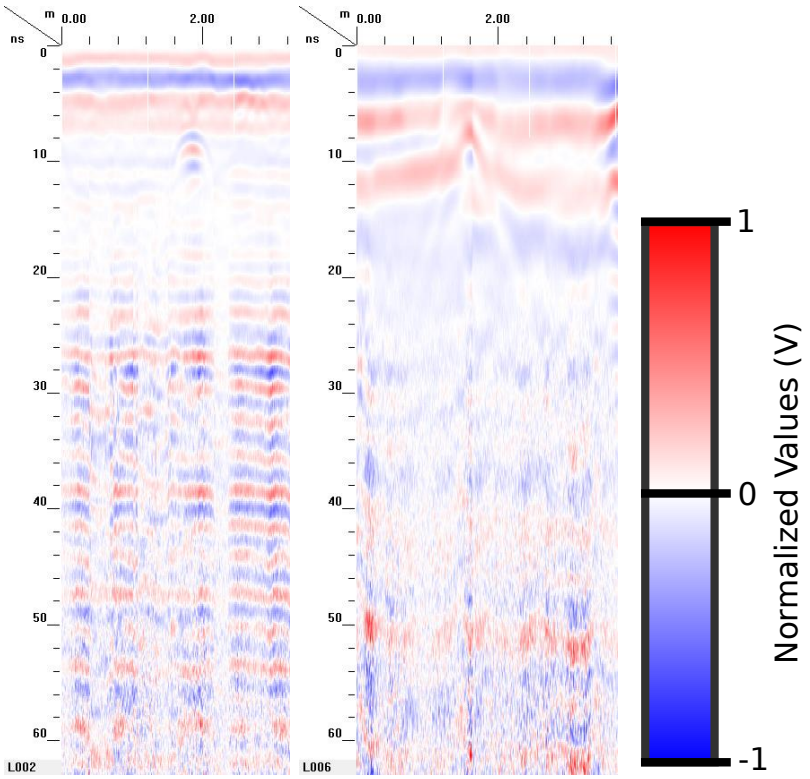

(a) (b) (c)

Figure 10.9: GPR B-scans for (a) short cross-polarized tag at 45° at 400 MHz, (b) at 200 MHz and (c) GPR key.

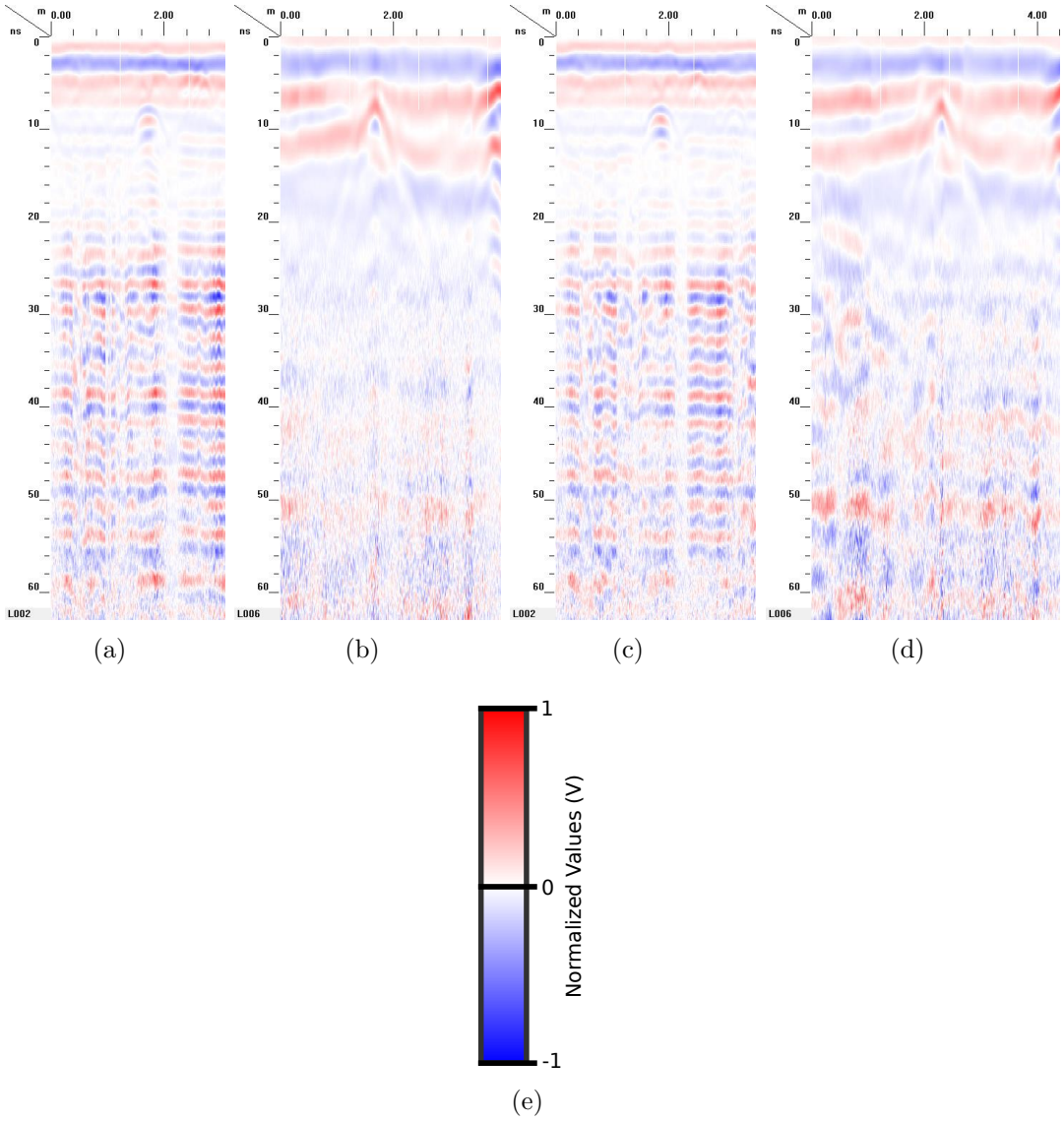

(a) (b) (c) (d)

(e)

Figure 10.10: GPR B-scans for (a) Bowtie foil tag at 45° at 400 MHz, (b) at 200 MHz,(c) Bowtie spray paint tag at 45° at 400 MHz, (d) at 200 MHz and (e) GPR key.

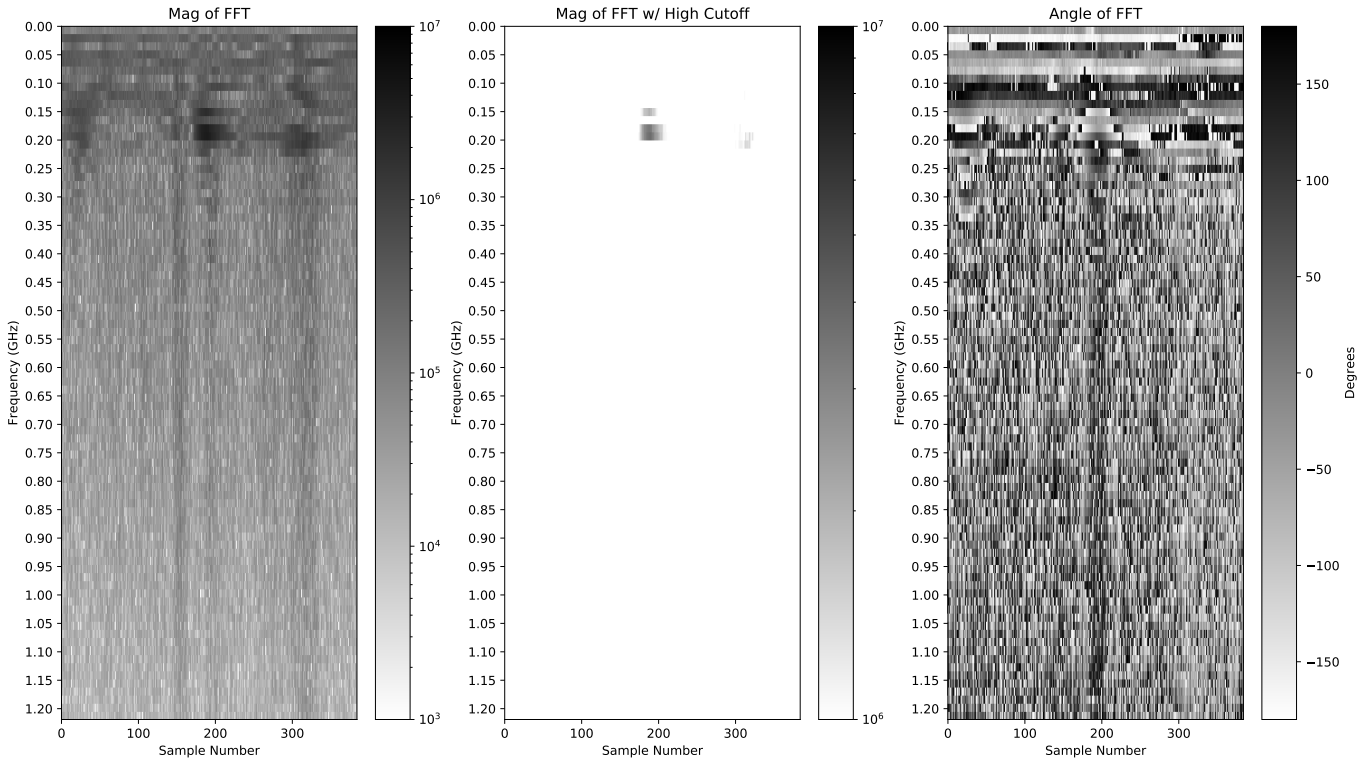

(a)

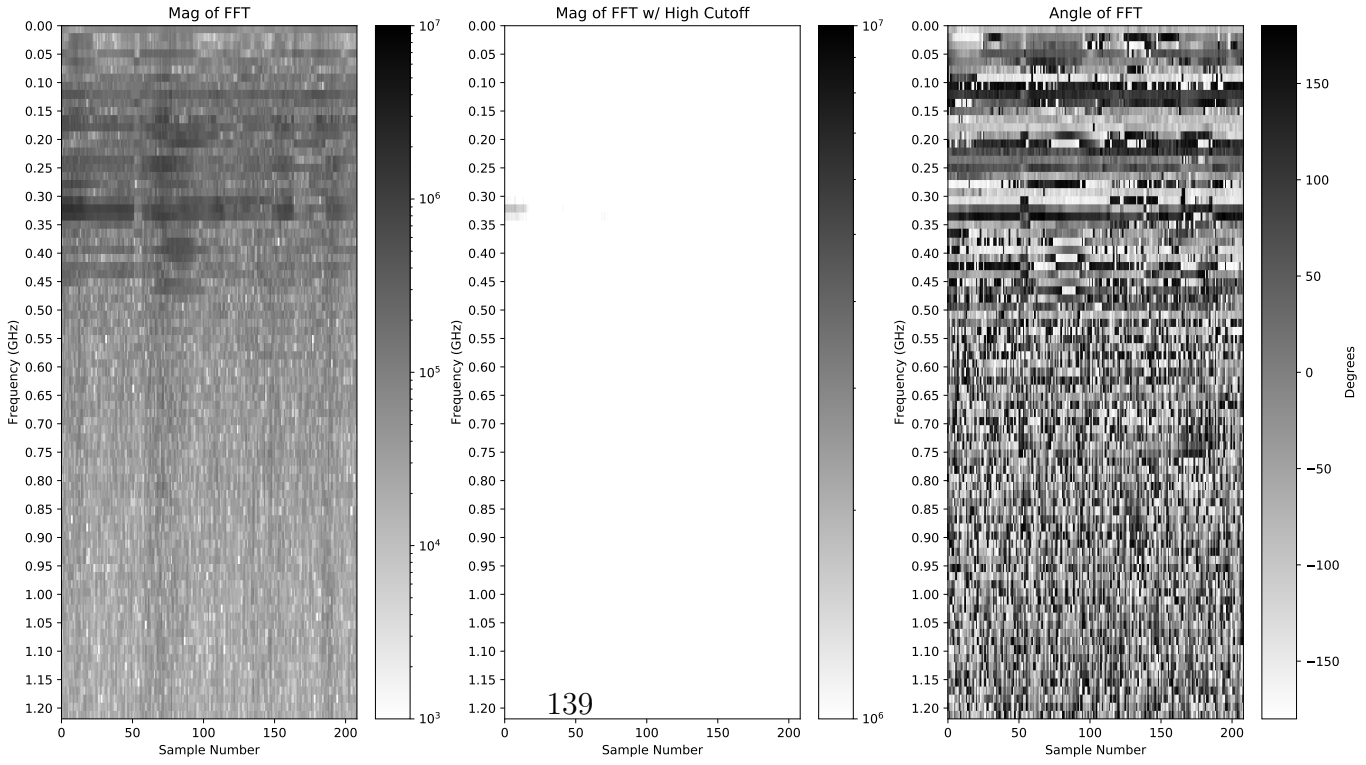

(b)

Figure 10.11: FFTs for long cross-polarized tags at (a) 200 MHz and (b) 400 MHz.

10.0.3 Polarization Independent Tags

The reason polarization independent tags are needed is two fold, first, it is simply due to GPR polarization limitation and second, the other is due to how a user scans with the GPR. Most commercial GPR systems are limited to only one polarization, therefore if the simple delay tag line is used, the performance will be minimized by any polarization mismatch. To accommodate this situation, many GPR users run two scans over the same area, with the second run collecting data from scans that are perpendicular to the first. In the case of these tags, if the second run is not implemented, the tags, if perpendicular to the GPR will not be noticed due to polarization mismatch. This can be noted in Fig. 10.12, where three scans of the simple long delay tag are compared. Although the tags are still quite noticeable when oriented at 45°, the response drops off sharply when at 90°. However as previously mentioned, this can be minimized with a polarization independent tag similar to Fig. 10.15. These polarization independent tags also have similar FFTs as noted in 10.14 with responses at 175 MHz and 350 MHz. If the true cross polarization response was recorded the FFT and and A-scan responses would be stronger and more pronounced.

10.1 Comparison of Metallic and cPE Tags

All previous testing and simulation of antennas occurred in air because of the difficulties in simulating soil conditions. To determine the performance of these antennas in expected service conditions, a test bed was constructed which allowed for easy

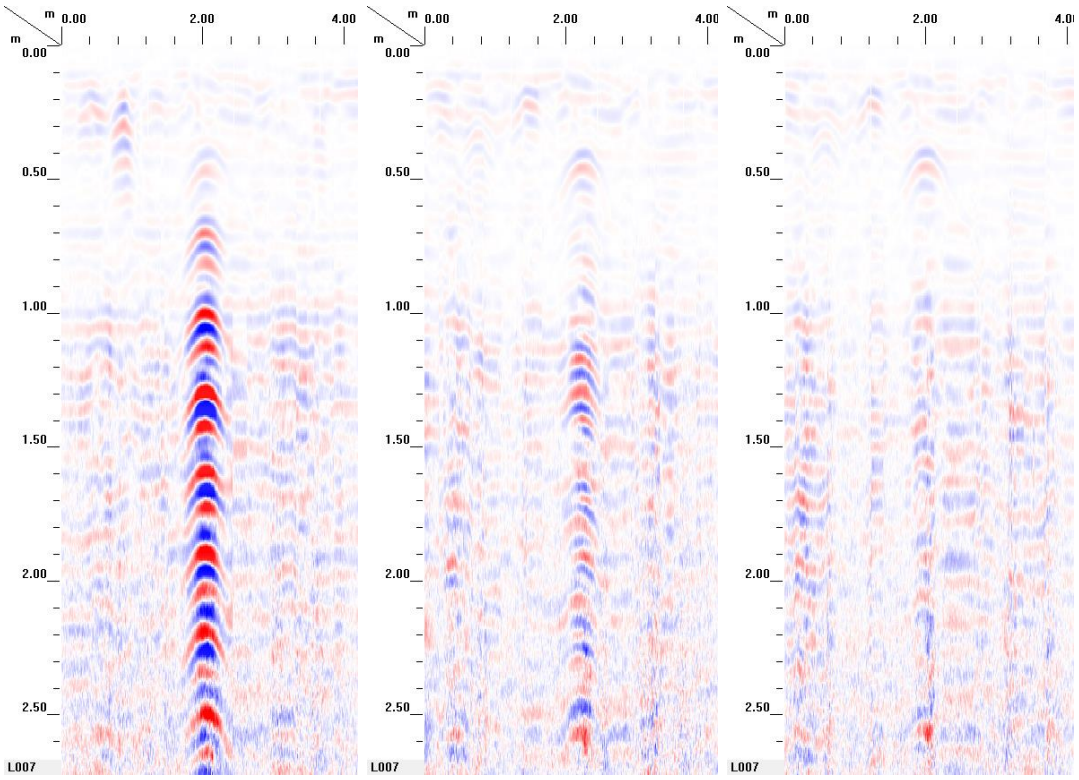

(a) (b) (c)

(d)

Figure 10.12: GPR B-scans for (a) Simple long delay line tag at 0° , (b) at 45° , (c) at 90° and (d) GPR key.

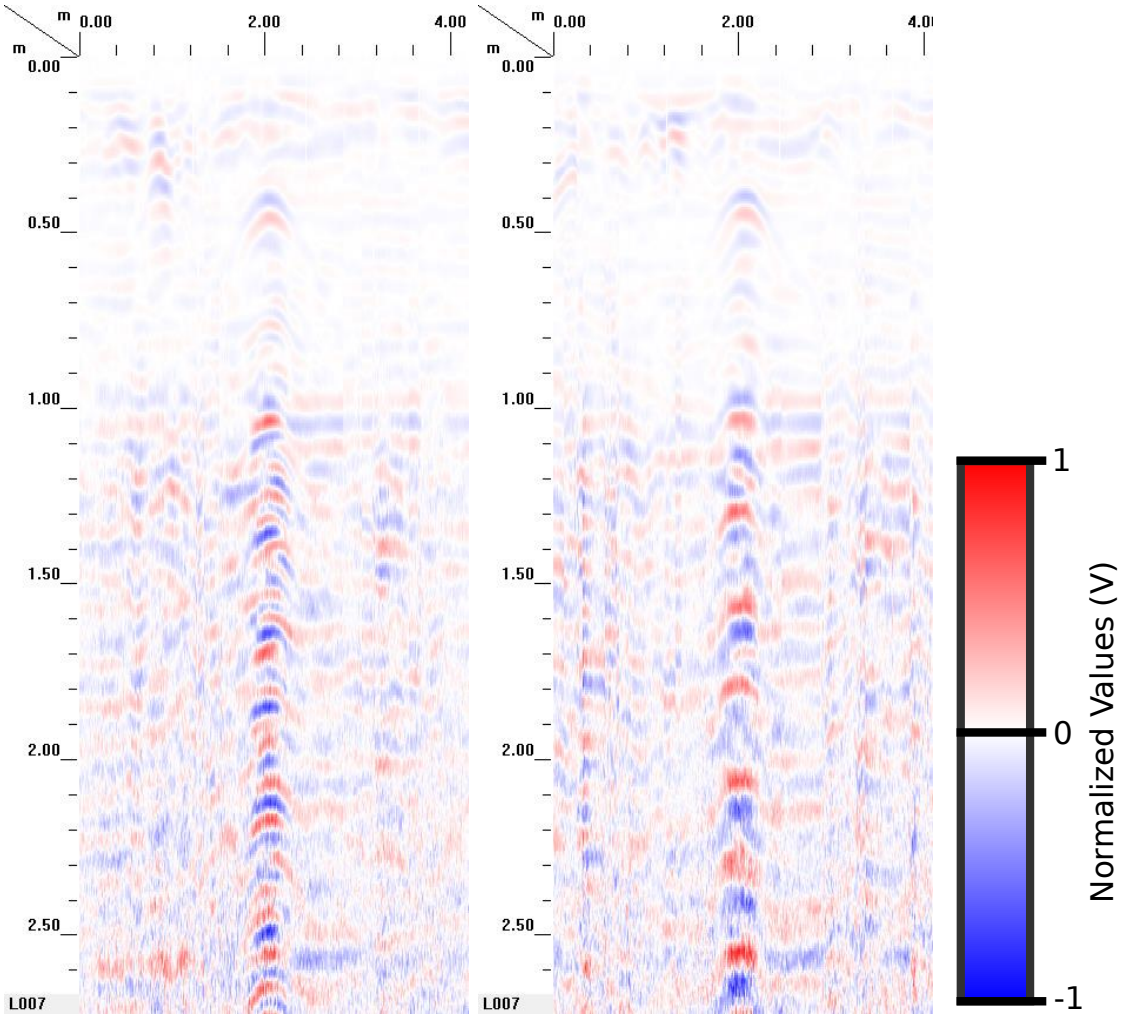

(a) (b) (c)

Figure 10.13: GPR B-scans for (a) polarization independent delay line tag at 0° , (b) at 45° and (c) GPR key

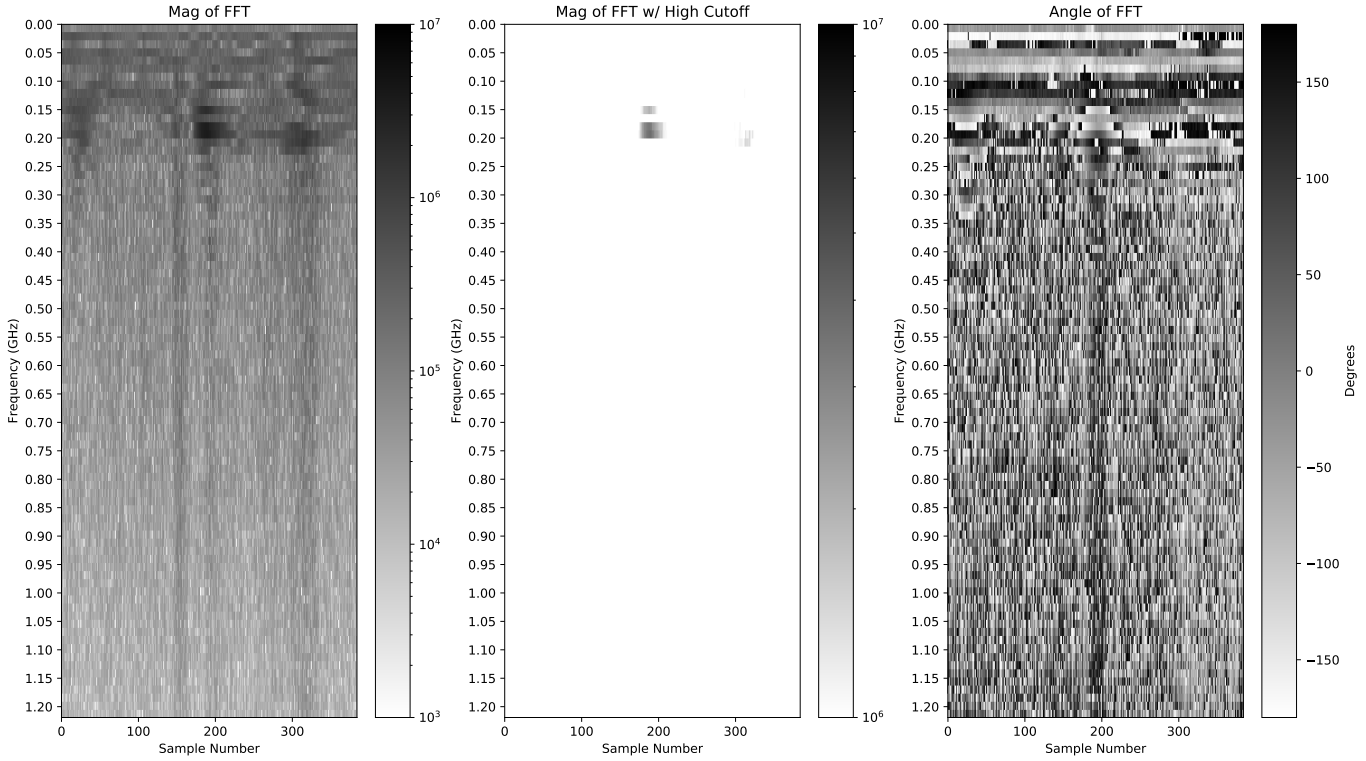

(a)

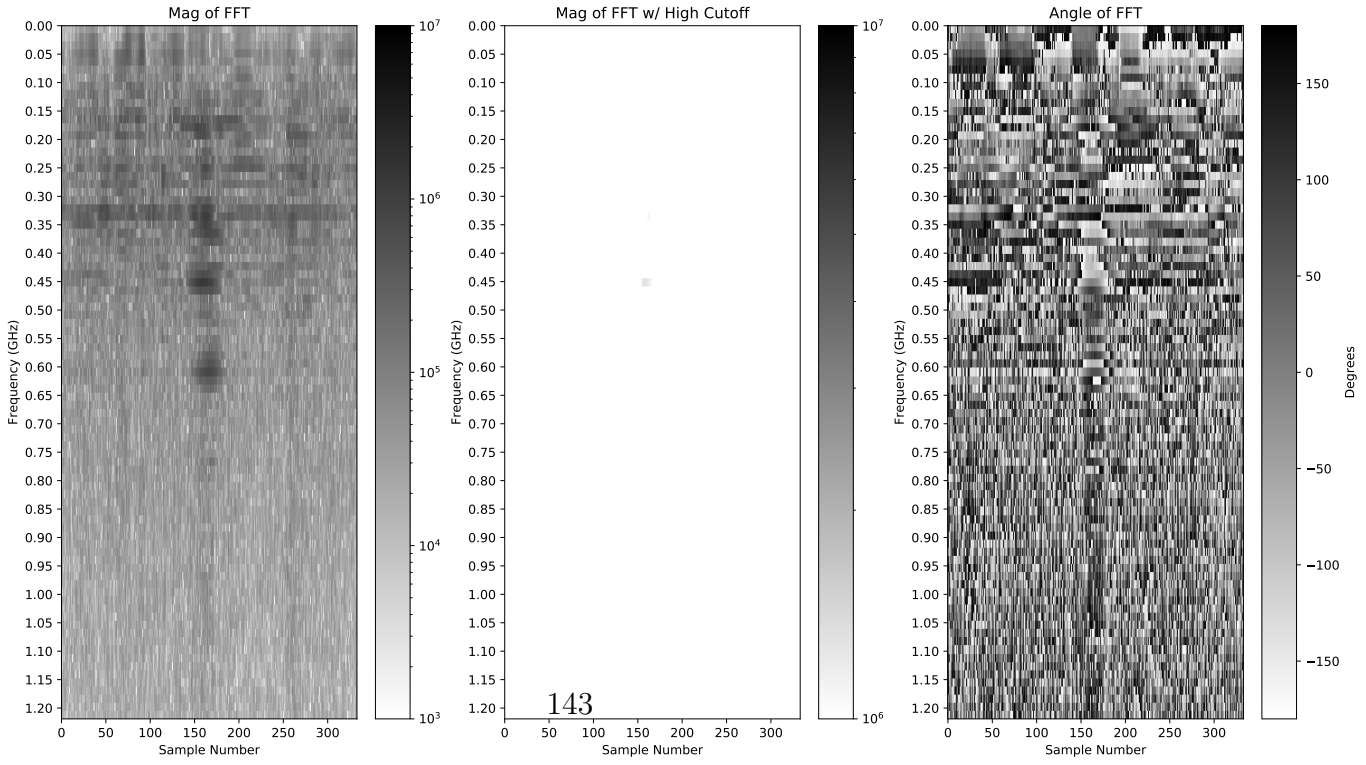

(b)

Figure 10.14: FFTs for long polarization independent tags at (a) 200 MHz and (b) 400 MHz.

installation of antennas with a thermoplastic pipe buried to standard regulation depths. Conduits connected the ends of the pipes with the surface such that antennas could easily be installed in the pipe for testing and measurement. A commercial ground penetrating radar unit with a 200 MHz antenna was used to survey the ground in paths perpendicular to the pipe. Doped polyethylene bowtie antennas and aluminum cross polarization antennas, some of which can be seen in Fig. 10.15, were inserted into the pipe and measured with the GPR unit.

Figure 10.15: A sample of the antennas used for testing. (1) A cross polarization antenna (2) Electroactive polyethylene double bowtie antenna (3) Time delay antennas (4) Electroactive polyethylene single bowtie antenna.

Results from the radar scans of the test bed are shown in Fig. 10.16. These graphs show a cross section of the ground taken in a straight line perpendicular to the pipe, with the horizontal axis representing the distance walked and the vertical axis displaying the time delay of the returned signal. On all three graphs, the location of the pipe is in the center of the scan. The response of the control scan of the pipe is lower in magnitude than that of either of the responses of the antennas. The response of the aluminum cross polarization antenna is stronger than that of the doped polyethylene bowtie, but both responses are much larger than that of the pipe with no antenna. Future work will include optimizing the antenna sizes for

application on small distribution lines while still resonating in ranges detectable with commercial ground penetrating radar.

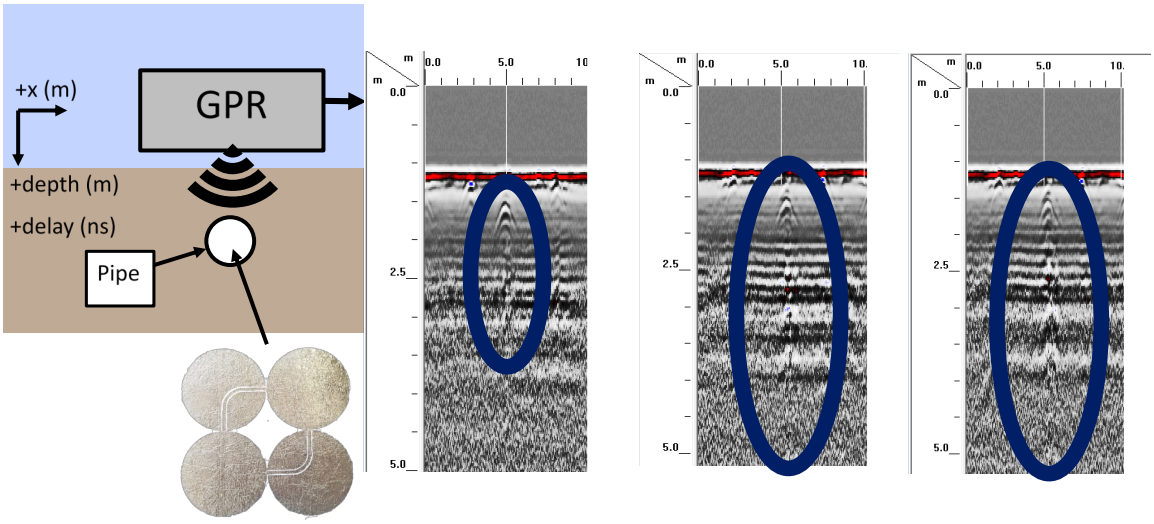

Figure 10.16: Results from ground penetrating radar testing of the testbed. (Left) Schematic of the underground test bed. (Second) Control test of the pipe with no antenna. (Third) The pipe with an electroactive polyethylene bowtie antenna. (Right) The pipe with an aluminum cross polarization antenna.

10.2 Discussion

Although all three types of tags all function to a certain degree, objectively the simple delay line tag still outperforms over the two other types in these underground tests. To a certain extent, this is a continuation from evaluating the previous antenna desings. The CP tag might be great if tested with specialized equipment, like Feng's cross polarized GPR, and these tags do work to a certain extent even with some polarization mismatch [27]. However with the standard equipment, the only

response that exists out of all three in this category is the longest delayed CP tag. Even then, this tag barely manages to send responses above the noise floor. This leads to the polarization independent tag, which still has a smaller response than the simple delay line tags. These tags work perfectly fine in any polarization, but this more complicated design could be mitigated by training the operator to go across the area in both polarizations. This polarization independent design also suffers from drawbacks when resonating due to the odd near field responses from the clover leaf antenna design, producing misshapen patterns in the GPR B-scan. If only one circular polarized antenna, using transmission lines with opens or shorts, was used instead of two linearly polarized antenna, like the tags from Shen, then the cross polarized tags could have resonated more [56]. However, since the higher dielectric constant from the soil renders previously circular polarized antennas to a linear polarization, this can a difficult issue to overcome which will need further investigation outside of this study. Therefore, the best tag out of these is the simple delay line tag with strong resonating patterns that last for more than 50 ns. The only tag comparison that can be made, for the resonating feature, is most likely Friedt's tag that used a delay of several microseconds with a SAW IC, where he saw more distinct multiple responses, since that delay was at least 10 times longer, after the tag's secondary response [28]. Additionally since these simple delay line tags can be serialized in a row and parallelized with each row side by side, they will be able to produce a greater response along the length of the pipe, along with being able to utilize open and closed circuits just as Dardari utilizes [22].

Chapter 11

Conclusion

Varying potential technologies were identified and described that could be used to distinguish underground objects more than what had been as noted in chapter 1 and 2. It was noted that there is potential use for frequency varying tags and other chip based designs. The time delay technology seemed to be one of the most viable, due to the use of commercially available GPR systems, cheap implementations of the technology using simple techniques, and easily understandable concepts.

Simulations of free space and in ground environments optimized designs for the proposed time delay tags within the third chapter. Simulation results indicated that antenna patterns bias heavily towards the dielectric with the greater dielectric constant when in a half space. Simulations also revealed that the dielectric detunes the reflection parameters of the antenna and transmission line to varying degrees, while also electrically lengthening both antenna and transmission lines. After transmission lines and antennas combine, expected secondary responses occurred according to

the physical length of the transmission lines. An alternative within this included investigation of cross polarization values which could indicate potential usefulness of some of these tags that use two antennas instead of one, however this would also be used with a custom GPR system with a cross polarization capability.

The manufacturing process of the tags in the third chapter led up to the setup of the experiments in the fourth chapter. These tags were first evaluated with the antennas themselves on a small antenna range. After verification of the effects on both antenna patterns and S parameters, a free space test setup quickly verified the viability of the tags. Those tags deemed viable would then be evaluated under day in the life use cases in an underground environment.

Experiments using the test setups in were then carried out to verify how environments affect antennas and test tags in free space and underground in the fifth chapter. The antenna range indicated that simulations from Chapter 3 were correct knowing that the dielectric biases the antenna. The free space setup results indicated that, even with the primary response from the larger pipe, the secondary response from the tags stood out from the noise and are clearly identifiable where the underground testbed resulted in some favorable results. Not only were the secondary responses recorded, but also the third, fourth and so on, since the tags themselves almost resonate. This was due to a heavy enough mismatch between the CPW and antenna, thus resulting in a noticeable frequency response that differentiated the individual tags even more. However, the responses from the short cross polarized tag and bowtie tag tests did not indicate reliability, not yielding promising results, save for the long CP tag. However, polarization independent tags in free space and underground environments yielded

promised results of being able to identify it without any regards to polarization mismatch.

In addition to the antenna characterization work, this project report presents two methods for imparting polyethylene with electromagnetic properties such that the pipes could be more easily detectable while in service. Polyethylene was doped with carbon black and aluminum to create a material conductive enough that it could be used to create antennas. These antennas were detected with ground penetrating radar in free space. The magnitude of the radar response decreased from that of a steel antenna of the same dimensions, but was still clearly distinguishable above the baseline polyethylene pipe. The addition of such high quantities of dopants gave the polyethylene brittle behavior, which could be seen in tensile tests. As the strain on a sample of doped PE increased, the resistance across the sample increased as well. Strain on a pipe was measured, and though an antenna on the pipe should survive at long term strains, it would likely sustain damage at the more extreme strains experienced during transportation and installation.

Conductive polyethylene antennas were designed to be applied to a 4" pipe, but the the most difficult pipes to detect underground are the smaller pipes that run to individual houses, so antennas must be designed for these smaller 1" pipes. The density of antennas that must be applied to a pipe for reliable detection over the length of the pipe can be quantified for different sizes of antennas. Soil can also affect the electromagnetic response of an antenna, so the polyethylene antennas should be installed and detected with the ground penetrating radar in soil.

For the mechanical properties of the doped polyethylene, the bilayer tensile test

should be repeated with layer thickness ratios more similar to the actual thickness ratio of an antenna on a pipe wall, because the results of the tensile test were highly dependent on the ratio of the two material thicknesses. If the brittle fracture that propagates through the neat polyethylene layer continues, methods to slow the rapid crack propagation will be developed. One approach is to mold a material that bonds less well to polyethylene between the two layers to stop the crack from penetrating into the neat polyethylene. Another method is to pre-crack the specimens so the crack cannot propagate quickly into the neat polyethylene. For the magnetic particles in the polyethylene, some thresholding will have to be done to determine what quantity of magnetic material is required for the polyethylene to be detectable underground. This can be used to quantify the amount of capsules that will be required for a given amount of polyethylene.

To date, all capsules have been layered into the polyethylene during compression molding. In pipe manufacturing, however, the polyethylene will be mixed through a Banbury mixer, so the microcapsules will have to be able to survive the mixing and extrusion processes. This process places higher shear on the capsules than the compression molding. Stronger capsules, such as dopamine coated double-walled capsules, which have been shown to survive at higher temperatures than the single-walled urea/formaldehyde capsules used in this work, are more likely to survive the higher temperatures and pressures of the polyethylene molding process.

In the long term, this capsule method could be expanded to impart self-healing inside the polyethylene. True self healing of thermoplastics has yet to be developed, as most healing requires external application of heat.

11.1 Tag Ranking

To judge and summarize the tags between other underground detection technologies, Table 11.1 visually displays the differences between the tags, regular GPR, a 3M RFID tag, and a tracer wire. Overall the simple delay line tags are still the most viable tags out of the three types of tags. The simple tag can easily carry more information in both wider varying lengths and being able to open and close terminating circuits when compared to the cross polarization tags. These single polarization simple tags also produce larger signal returns than the polarization independent tags—even if the user is required to scan in both X and Y directions then, especially when the size of the simple tag takes up less room on the pipe. This in hand brings the possibility of using simple delay lines tags on much deeper pipes. That is using these tags where lower frequencies like 25 or 50 MHz GPRs might be needed. However this type of delay tag would involve much more than a single layer CPW and would need to be further investigated.

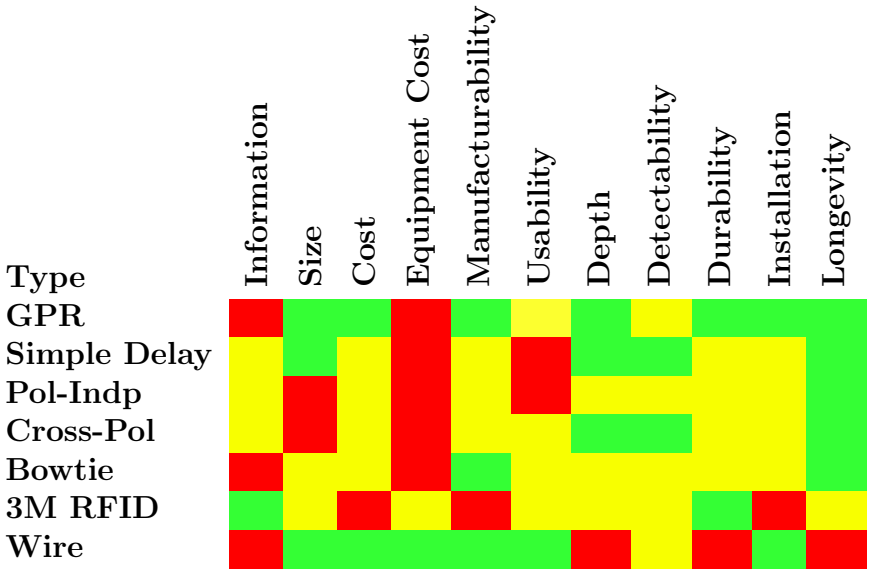

Table 11.1: Comparisons between other underground locating methods — including regular GPR, RFID tags, and wires — and this work. Green is better and red is worse.

Bibliography

[1] Application note: Cycling endurance and data retention of EEPROMs in ST25DVxxx products based on CMOS F8H process.

[2] Chapter 2 Inspections , Tests and Safety Considerations. In *Handbook of Polyethylene Pipe*, chapter 2, pages 15–41.

[3] Chapter 3 Material Properties. In *Handbook of Polyethylene Pipe*, chapter 3.

[4] Chapter 6 Design of PE Piping Systems. In *Handbook of Polyethylene Pipe*, chapter 6.

[5] Chapter 7 Underground Installation of PE Piping. In *Handbook of Polyethylene Pipe*, chapter 7, pages 265–303.

[6] Chapter 1 Introduction. In *Handbook of Polyethylene Pipe*, number 2, chapter 1, pages 5–13. 1950.

[7] ASTM D 5045: Standard Test Methods for Plane-Strain Fracture Toughness and Strain Energy Release. pages 1–9, 1999.

[8] ASTM D 638: Standard Test Method for Tensile Properties of Plastics. *ASTM Standards*, (January):1–15, 2004.

[9] S. Abrahamson, M. Bartha, H. F. Scott, J. Bungey, R. de Vekey, P. Hanninen, R. A. van Overmeeren, J. K. van Deen, S. Tillard, J. Fidler, D. L. Wilkinson, J. Cariou, G. Schaber, T. Haglars, and F. Nicollin. Ground Penetrating Radar. *IEE Radar Series*, 15:734, 2004.

[10] S. Abrahamson, M. Bartha, H. F. Scott, J. Bungey, R. de Vekey, P. Hanninen, R. A. van Overmeeren, J. K. van Deen, S. Tillard, J. Fidler, D. L. Wilkinson, J. Cariou, G. Schaber, T. Haglars, and F. Nicollin. Ground Penetrating Radar. *IEE Radar Series*, 15:734, 2004.

[11] Grzegorz Adamiuk, Thomas Zwick, and Werner Wiesbeck. Compact, dual-polarized UWB-antenna, embedded in a dielectric. *IEEE Transactions on Antennas and Propagation*, 58(2):279–286, 2010.

[12] Kevin N Adams. *Self Healing Composite for Dental Application.* PhD thesis, The University of Tulsa, 2015.

[13] Peter Annan. *Ground Penetrating Radar: Theory and Applications.* Elsevier, 1 edition, 2009.

[14] ASTM International. ASTM D 2321 Standard Practice for Underground Installation of Thermoplastic Pipe for Sewers. 04, 2000.

[15] ASTM International. ASTM D 3035 Standard Specification for Polyethylene (PE) Plastic Pipe (DR-PR) Based on Controlled. *Current*, pages 1–7, 2001.

[16] ASTM International. ASTM D 4703: Standard Practice for Compression Molding Thermoplastic Materials into Test Specimens , Plaques , or Sheets. pages 1–13, 2013.

[17] Harry Augenblick. Harmonic Detection System, 1969.

[18] Richard J Barton. Some Fundamental Limits on SAW RFID Tag Information Capacity and Collision Resolution. Technical report, 2014.

[19] E N Brown, M R Kessler, N R Sottos, and S R White. In situ poly(urea-formaldehyde) microencapsulation of dicyclopentadiene. *Journal of microencapsulation*, 20(6):719–30, 2003.

[20] Copperhead Industries LLC. Best Practices for Tracer Wire System Installation. Technical report.

[21] Matthew D. Crall. *Guided Placement of Magnetic Microcapsules in Self-Healing Polymeric Materials*. PhD thesis, The University of Tulsa, 2017.

[22] Davide Dardari, Raffaele D'Errico, Christophe Roblin, Alain Sibille, and Moe Z. Win. Ultrawide Bandwidth RFID : The Next Generation ? 98(9), 2010.

[23] Shuvashis Dey, Jhantu Kumar Saha, and Nemai Chandra Karmakar. Smart Sensing: Chipless RFID Solutions for the Internet of Everything. *IEEE Microwave Magazine*, 2015.

[24] Marlene H. Dortch. Revision of Part 15 of the Commission's Rules Regarding Ultra-Wideband Transmission Systems Petition. Technical Report 98, Federal Communications Commission, Washington, D.C, 2010.

[25] Peter J. Edmonson and Colin K. Campbell. DUAL TRACK SURFACE ACOUSTIC WAVE RFID/SENSOR RFID/SENSOR, 2006.

[26] Caixia Feng, Wenmei Zhang, Li Li, Liping Han, Xinwei Chen, and Runbo Ma. Angle-Based Chipless RFID Tag with High Capacity and Insensitivity to Polarization. *IEEE Transactions on Antennas and Propagation*, 2015.

[27] Xuan Feng, Yue Yu, Cai Liu, and Michael Fehler. Combination of H-Alpha Decomposition and Migration for Enhancing Subsurface Target Classification of GPR. *IEEE Transactions on Geoscience and Remote Sensing*, 53(9):4852–4861, 2015.

[28] J. M. Friedt, T. Rtornaz, S. Alzuaga, T. Baron, G. Martin, T. Laroche, S. Ballandras, M. Griselin, and J. P. Simonnet. Surface acoustic wave devices as passive buried sensors. *Journal of Applied Physics*, 109(3):1–10, 2011.

[29] Joshua D. Griffin, G.D. Durgin, A. Haldi, and B. Kippelen. RF Tag Antenna Performance on Various Materials Using Radio Link Budgets. *IEEE Antennas and Wireless Propagation Letters*, 5(1):247–250, 2006.

[30] E.O. Hammerstad and F. Bekkadal. A microstrip handbook. Technical report, University of Trondheim, 1975.

[31] E.O. Hammerstad and O. Jensen. Accurate models for microstrip computer-aided design. *1980 IEEE MTT-S Int. Microwave Symp. Dig.*, pages 407–409, 1980.

[32] Sanming Hu, Yuan Zhou, Choi Look Law, and Wenbin Dou. Study of a uniplanar monopole antenna for passive chipless UWB-RFID localization system. *IEEE Transactions on Antennas and Propagation*, 58(2):271–278, 2010.

[33] Haoping Huang and I. J. Won. Characterization of UXO-like targets using broadband electromagnetic induction sensors. *IEEE Transactions on Geoscience and Remote Sensing*, 41(3):652–663, 2003.

[34] Innovative Trench Solutions Inc. tracerwire, 2012.

[35] Sen Kang, Marta Baginska, Scott R. White, and Nancy R. Sottos. Core–Shell Polymeric Microcapsules with Superior Thermal and Solvent Stability. *ACS Applied Materials & Interfaces*, page 150513121149006, 2015.

[36] Lev Kofman, Amit Ronen, and Sam Frydman. Detection of model voids by identifying reverberation phenomena in GPR records. *Journal of Applied Geophysics*, 59(4):284–299, 2006.

[37] Samuel G Laney. *Development and Characterization of a Scanning System for a Magnetic Self-Sensing Composite*. PhD thesis, The University of Tulsa, 2018.

[38] Michael Mamoun. PIPELINE DAMAGE PREVENTION THROUGH THE USE OF LOCATABLE MAGNETIC PLASTIC PIPE WITH A UNIVERSAL LOCATOR. 2005.

[39] A P Moser. *Buried Pipe Design*. McGraw-Hill, second edition.

[40] Stanley Mruk. Plastic Pipe in Gas Distribution: Twenty-Five Years of Achievement. *Gas Industries*, 1985.

[41] C M Nijas, R Dinesh, U Deepak, Abdul Rasheed, S Mridula, K Vasudevan, and P Mohanan. Chipless RFID tag using multiple microstrip open stub resonators. *IEEE Transactions on Antennas and Propagation*, 60(9):4429–4432, 2012.

[42] Charles P Oden and Craig W Moulton. GP Workbench Manual : Technical Manual , User' s Guide , and Software Guide. Technical report, 2006.

[43] Charles P. Oden, Michael H. Powers, David L. Wright, and Gary R. Olhoeft. Improving GPR image resolution in lossy ground using dispersive migration. *IEEE Transactions on Geoscience and Remote Sensing*, 45(8):2492–2499, 2007.

[44] C Ozdemir, S Demirci, and E Yigit. Practical Algorithms To Focus B-Scan Gpr Images: Theory and Application To Real Data. *Progress In Electromagnetics Research B*, 6:109–122, 2008.

[45] Andrew J. Peacock. *Handbook of Polyethylene*. 2000.

[46] Performance Pipe. Technical Note PP 819-TN. (October 2007).

[47] Nadine Pesonen, Kaarle Jaakkola, Jerome Lamy, Kaj Nummila, and Jouko Marjone. Smart RFID Tags. In *Development and Implementation of RFID Technology*, number February, pages 159–178. I-Tech, Vienna, 2009.

[48] D.M. Pozar. *Microwave Engineering, 4th Edition*. Wiley, 2011.

[49] Stevan Preradovic, Isaac Balbin, Nemai Karmakar, and Gerry Swiegers. A novel chipless RFID system based on planar multiresonators for barcode replacement BT - 2008 IEEE International Conference on RFID (Frequency Identification),

IEEE RFID 2008, April 16, 2008 - April 17, 2008. *2008 IEEE International Conference on RFID*, 3169:289–296, 2008.

[50] Reza Rezaiesarlak and Majid Manteghi. Design of chipless RFID tags based on Characteristic Mode Theory (CMT). *IEEE Transactions on Antennas and Propagation*, 2015.

[51] Huaping Wang Richard Liu, Wei Ren and Chen Guo. Ground-Penetrating Radar. In *Principles of Modern Radar: Volume 3: Radar Applications*, pages 691–747. 2013.

[52] Mark A. Richards, James A. Scheer, and William A. Holm. *Principles of Modern Radar Vol 1.* 2010.

[53] Iulian Rosu. Microstrip, stripline, and cpw design. Technical report, QSL, 2016.

[54] Motoyuki Sato and Yasushi Iizuka. Cross Bow-Tie Antenna for Multistatic Ground Penetrating Radar. *Proceedings of ISAP*, pages 1092–1093, 2016.

[55] Hans G. Schantz. *The Art and Science of Ultrawideband Antennas.* Artech House, 2 edition, 2015.

[56] Yizhu Shen and Choi Look Law. A Low-Cost UWB-RFID System Utilizing Compact Circularly Polarized Chipless Tags. 11(c):1382–1385, 2012.

[57] Michael Steer. *Microwave and RF Design A Systems Approach.* Scitech Publishing, 2nd edition, 2013.

[58] W.E. Thain. Determination of the Best Ground Penetrating Radar Source Signal Type for the Accurate Location of Underground Utilities. Technical report, SYNTEK Engrg & Computer Systems, Inc., 1988.

[59] Michelle Thompson. 3D Printed 122GHz Cassegrain Assembly by Michelle W5NYV. In *Microwave Update*, pages 86–99, 2017.

[60] Arnaud Vena, Etienne Perret, Smail Tedjini, Guy Eymin Petot Tourtollet, Anastasia Delattre, Frédéric Garet, and Yann Boutant. Design of chipless RFID tags printed on paper by flexography. *IEEE Transactions on Antennas and Propagation*, 2013.

[61] H. A. Vidya. Radar Imaging of Concealed Targets. *International Journal of Computer Science and Information Technologies*, 5(4):5192–5196, 2014.

[62] Craig Warren, Antonios Giannopoulos, and Iraklis Giannakis. gprMax: Open source software to simulate electromagnetic wave propagation for Ground Penetrating Radar. *Computer Physics Communications*, 209:163–170, 2016.

[63] Y.F. Weng, S. W. Cheung, T. I. Yuk, and L. Liu. Design of Chipless UWB RFID System Using A CPW Multi-Resonator. 55(1):13–31, 2013.

[64] Seniha Esen Yuksel, Jeremy Bolton, and Paul Gader. Multiple-Instance Hidden Markov Models With Applications to Landmine Detection. *IEEE Transactions on Geoscience and Remote Sensing*, 53(12):6766–6775, 2015.

Code

The code below takes in a set of .csv files and stacks them to easily compare differences between A-scans.

Listing 1: A-scan Stacked Plot Python Example

```
import tkinter as tk
from tkinter import filedialog
from numpy import array, hstack, vstack, genfromtxt
import numpy as np
import matplotlib as mp
import matplotlib.pyplot as plt
import matplotlib.gridspec as gridspec
import matplotlib.ticker as tick
from scipy import *
from scipy.signal import butter, lfilter


root = tk.Tk()
root.withdraw()
file_path = filedialog.askopenfilename()
# file_path2 = filedialog.askopenfilename()
# file_path3 = filedialog.askopenfilename()


data = genfromtxt(file_path, delimiter='\t', skip_header=1)
# data3 = genfromtxt(file_path3, delimiter=' ', skip_header=14)
```

```
Ascan1 = np.zeros(shape=(len(data)-1))
time = np.zeros(shape=(len(data)-1))

time = data[:, 0]
Short = data[:, 1]
Shortperp = data[:, 2]
Crosspol = data[:, 3]
Crosspol45 = data[:, 4]
Nothing = data[:, 5]
Pipe = data[:, 6]
PolIndp = data[:, 7]
Long = data[:, 8]
Longperp = data[:, 9]



# test3 = data3[:, 3] + 1j*data3[:, 4]
# Ascan3 = -np.array(iczt(np.hanning(m)*test3, m, w, a))



# plt.plot(t, Ascan1, 'r', t, Ascan2, 'b', t, Ascan2-Ascan1, 'g')
# plt.plot(t*scaling, Ascan2-Ascan1)
```

```
# plt.plot(t*scaling, Ascan1)
# fig = plt.figure(figsize=(3.5, 1), dpi=600)
# fig = plt.plot(t*scaling, Ascan2-Ascan1)

# plt.show()
font = {'family': 'Times New Roman',
'weight': 'normal',
'size': 8
}

lines = {'linewidth': '1',
'c': 'red'
}


mp.rc('font', **font)
mp.rc('lines', **lines)

gs = gridspec.GridSpec(7, 1)
fig = plt.figure(figsize=(3.5, 3), dpi=300)

ax = fig.add_subplot(gs[0])
for axis in ['top', 'bottom', 'left', 'right']:
```

```
ax.spines[axis].set_linewidth(0.5)
ax.plot(time, (Pipe)*1000, 'black')
ax.grid(True)
ax.yaxis.set_major_locator(tick.MultipleLocator(.1))
# ax.yaxis.set_minor_locator(tick.MultipleLocator(.1))
ax.xaxis.set_major_locator(tick.MultipleLocator(5))
ax.xaxis.set_minor_locator(tick.MultipleLocator(1))
# ax.axes.get_xaxis().set_visible(False)
ax.set_ylim([-.15, .15])
ax.text(22, .14, 'PVC Pipe', ha='center', va='top')

ax = fig.add_subplot(gs[1])
for axis in ['top', 'bottom', 'left', 'right']:
ax.spines[axis].set_linewidth(0.5)
ax.plot(time, (Short)*1000, 'black')
ax.grid(True)
ax.yaxis.set_major_locator(tick.MultipleLocator(.1))
# ax.yaxis.set_minor_locator(tick.MultipleLocator(.1))
ax.xaxis.set_major_locator(tick.MultipleLocator(5))
ax.xaxis.set_minor_locator(tick.MultipleLocator(1))
ax.set_ylim([-.15, .15])
ax.text(22, .14, 'Short Simple Delay Line', ha='center', va='top')
```

```
ax = fig.add_subplot(gs[2])
for axis in ['top', 'bottom', 'left', 'right']:
ax.spines[axis].set_linewidth(0.5)
ax.plot(time, (Long)*1000, 'black')
ax.grid(True)
ax.yaxis.set_major_locator(tick.MultipleLocator(.1))
# ax.yaxis.set_minor_locator(tick.MultipleLocator(.1))
ax.xaxis.set_major_locator(tick.MultipleLocator(5))
ax.xaxis.set_minor_locator(tick.MultipleLocator(1))
ax.set_ylim([-.15, .15])
ax.text(22, .14, 'Long Simple Delay Line', ha='center', va='top')

ax = fig.add_subplot(gs[3])
for axis in ['top', 'bottom', 'left', 'right']:
ax.spines[axis].set_linewidth(0.5)
ax.plot(time, (Longperp)*1000, 'black')
ax.grid(True)
ax.yaxis.set_major_locator(tick.MultipleLocator(.1))
# ax.yaxis.set_minor_locator(tick.MultipleLocator(.1))
ax.xaxis.set_major_locator(tick.MultipleLocator(5))
ax.xaxis.set_minor_locator(tick.MultipleLocator(1))
ax.set_ylim([-.15, .15])
```

```
ax.text(22, .14, 'Long Simple DL Polarization Mismatch'
, ha='center', va='top')

ax = fig.add_subplot(gs[4])
for axis in ['top', 'bottom', 'left', 'right']:
ax.spines[axis].set_linewidth(0.5)
ax.plot(time, (PolIndp)*1000, 'black')
ax.grid(True)
ax.yaxis.set_major_locator(tick.MultipleLocator(.1))
# ax.yaxis.set_minor_locator(tick.MultipleLocator(.1))
ax.xaxis.set_major_locator(tick.MultipleLocator(5))
ax.xaxis.set_minor_locator(tick.MultipleLocator(1))
ax.set_ylim([-.15, .15])
ax.text(22, .14, 'Long Polarization Independent DL',
ha='center', va='top')

ax = fig.add_subplot(gs[5])
for axis in ['top', 'bottom', 'left', 'right']:
ax.spines[axis].set_linewidth(0.5)
ax.plot(time, (Crosspol)*1000, 'black')
ax.grid(True)
ax.yaxis.set_major_locator(tick.MultipleLocator(.1))
# ax.yaxis.set_minor_locator(tick.MultipleLocator(.1))
```

```
ax.xaxis.set_major_locator(tick.MultipleLocator(5))
ax.xaxis.set_minor_locator(tick.MultipleLocator(1))
ax.set_ylim([-.15, .15])
ax.text(22, .14, 'Long CP DL', ha='center', va='top')

ax = fig.add_subplot(gs[6])
for axis in ['top', 'bottom', 'left', 'right']:
ax.spines[axis].set_linewidth(0.5)
ax.plot(time, (Crosspol45)*1000, 'black')
ax.grid(True)
ax.yaxis.set_major_locator(tick.MultipleLocator(.1))
# ax.yaxis.set_minor_locator(tick.MultipleLocator(.1))
ax.xaxis.set_major_locator(tick.MultipleLocator(5))
ax.xaxis.set_minor_locator(tick.MultipleLocator(1))
ax.set_ylim([-.15, .15])
ax.text(22, .14, 'Long CP DL Rotated 45 degrees',
ha='center', va='top')

fig.text(0.5, 0.02, 'Time (ns)', ha='center', va='center')
fig.text(0.02, 0.5, 'Response(mV)', ha='center',
va='center', rotation='vertical')
fig.tight_layout(h_pad=-1.5)
plt.savefig('Ascan_simpleall.pdf')
```

```
plt.show()
```

This code creates a B-scan out of numbered .csv files which is derived from the part of the code from C. Warren and A. Giannopoulos's simulation software gprMax [62].

Listing 2: B-scan Python Example

```
import tkinter as tk
from tkinter import filedialog
from numpy import genfromtxt
import numpy as np
import matplotlib.pyplot as plt
import matplotlib as mp


root = tk.Tk()
root.withdraw()
file_path = filedialog.askopenfilename()



def fkmig(data):
c = 3*10**8
[t0, d0] = len(data)



def Bscanimg(bimg):
bimg = np.real(bimg)
```

```
fig = plt.figure(figsize=(3.5, 2), facecolor='w',
edgecolor='w', dpi=300)
scaling = 15/len(bimg)+10

font = {'family': 'Times New Roman',
'weight': 'normal',
'size': 8
}
mp.rc('font', **font)
plt.imshow(bimg*1000, extent=[0, bimg.shape[1],
bimg.shape[0], 0], interpolation='hanning', aspect='auto',
cmap='seismic', vmin=-np.amax(np.abs(bimg))*1000,
vmax=np.amax(np.abs(bimg))*1000)
# Thanks to gprMax's B-scan code from Craig Warren
 & Antonis Giannopoulos
plt.xlabel('Trace number')
plt.ylabel('Time [ns]')
plt.yticks([0, 666, 1331, 1997, 2663, 3228, 3994, 4660, 5325,
 5991, 6657], [15, 16, 17, 18, 19, 20, 21, 22, 23, 24, 25])

#plt.axes([1, 11, 25, 10])
# plt.title('{}'.format(filename))
plt.grid()
```

```
cb = plt.colorbar(label='Response (mV)')
plt.savefig('Bscan_Simple.pdf')
plt.show()



start_n = 1
n = 11

data = genfromtxt(file_path, delimiter='\t', skip_header=1)
Bscan = data[:, 1:n+1]
time = data[:, 0]

m = 6657

BscanS = np.fft.fft2(Bscan)

for ky in range(1, n):
for w in range(1, m+1):
kz = (w**2/(3*10**8)**2-ky**2)**.5
S = 3*10**8/2*kz/(ky**2+kz**2)**.5
BscanS[w-1, ky-1] = BscanS[w-1, ky-1]*S
```

```
BscanS = np.fft.ifft2(BscanS)


Bscanimg(Bscan)
```

This code creates FFTs of each individual A-scan and compiles them similarly to the B-scan code. However this code takes .csv files transferred from GP Workbench [42].

Listing 3: FFT graphs converted from B-scans

```
import numpy as np
import numpy.fft as fft
import matplotlib.pyplot as plt
from matplotlib.colors import LogNorm

filename="/file.csv"



reader = np.loadtxt(filename, dtype=float,
delimiter=',', skiprows=2, usecols=range(4, 512))

rows = len(reader)
print(rows)

n = 512-4

print(reader)

#plt.imshow(reader, cmap='RdBu', interpolation='nearest',
```

```
 aspect='equal')
#plt.show()

transformed = fft.rfft(reader)
transformed = np.rot90(transformed, k=3)

ticks = np.arange(0, 1/(70/512)/2/3, 0.05)

fig, ((ax1), (ax2), (ax3)) = plt.subplots(1, 3, figsize=(18, 10))

T1 = ax1.imshow(np.abs(transformed), cmap='binary',
 interpolation='nearest', aspect='auto', extent=[0,
 rows, 1/(70/512)/2/3, 0], norm=LogNorm(vmin=1e3,  vmax=1e7))

plt.sca(ax1)
plt.yticks(ticks)
plt.title("Mag of FFT")
plt.ylabel("Frequency (GHz)")
plt.xlabel("Sample Number")
fig.colorbar(T1, ax=ax1)
#end of Mag of FFT plot

T2 = ax2.imshow(np.abs(transformed), cmap='binary',
```

```
 interpolation='nearest', aspect='auto', extent=[0,
  rows, 1/(70/512)/2/3, 0], norm=LogNorm(vmin=1e6,  vmax=1e7))

plt.sca(ax2)
plt.yticks(ticks)
plt.title("Mag of FFT w/ High Cutoff")
plt.ylabel("Frequency (GHz)")
plt.xlabel("Sample Number")
fig.colorbar(T2, ax=ax2)
#end of Mag of FFT Hight cutoff plot

T3 = ax3.imshow(np.angle(transformed, deg=1), cmap='binary',
 interpolation='nearest', aspect='auto', extent=
 [0, rows, 1/(70/512)/2/3, 0])


plt.sca(ax3)
plt.yticks(ticks)
plt.title("Angle of FFT")
plt.ylabel("Frequency (GHz)")
plt.xlabel("Sample Number")
fig.colorbar(T3, ax=ax3, label="Degrees")
#end of Angle of FFT
```

```
plt.savefig("/home/logic/Pictures/FFT/OutputPlot.pdf",
 bbox_inches='tight')
plt.show()
```

List of GPR Tests

Test	Tag Type	Frequency (MHz)	Angle (°)	Material	Date	Notes
81	Pipe	400	0	N/A	10 Jan 2018	
82	Pipe	400	0	N/A	10 Jan 2018	
86	Pol Indp	400	0	Foil	10 Jan 2018	
87	Pol Indp	400	0	Foil	10 Jan 2018	
88	Short CO	400	0	Foil	10 Jan 2018	
89	Short CO	400	0	Foil	10 Jan 2018	
90	Long CO	400	0	Foil	10 Jan 2018	
91	Long CO	400	0	Foil	10 Jan 2018	Along Trench Access
92	Long CO	400	0	Foil	10 Jan 2018	
93	Long CO	400	0	Foil	10 Jan 2018	
94	Pipe	400	N/A	N/A	24 Jan 2018	
95	Long CP	400	45	Foil	24 Jan 2018	
96	Bowtie	400	45	Foil	24 Jan 2018	
97	Bowtie	400	45	Paint	24 Jan 2018	
98	Short CP	400	45	Foil	24 Jan 2018	

99	Pipe	200	N/A	N/A	31 Jan 2018
100	Pipe	200	N/A	N/A	31 Jan 2018
101	Short CO	200	0	Foil	31 Jan 2018
102	Short CO	200	0	Foil	31 Jan 2018
103	Long CO	200	0	Foil	31 Jan 2018
104	Long CO	200	0	Foil	31 Jan 2018
105	Pol Indp	200	0	Foil	31 Jan 2018
106	Pol Indp	200	0	Foil	31 Jan 2018
107	Long CP	200	45	Foil	31 Jan 2018
108	Long CP	200	45	Foil	31 Jan 2018
109	Pipe	200	N/A	N/A	7 Feb 2018
110	Pipe	200	N/A	N/A	7 Feb 2018
111	Long CP	200	45	Foil	7 Feb 2018
112	Long CP	200	45	Foil	7 Feb 2018
113	Bowtie	200	45	Paint	7 Feb 2018
114	Bowtie	200	45	Paint	7 Feb 2018
115	Long CO	200	45	Foil	7 Feb 2018
116	Long CO	200	45	Foil	7 Feb 2018
117	Bowtie	200	45	Foil	7 Feb 2018
118	Bowtie	200	45	Foil	7 Feb 2018
119	Short CP	200	45	Foil	7 Feb 2018
120	Short CP	200	45	Foil	7 Feb 2018
127	Pipe	400	N/A	N/A	7 Mar 2018

128	Pipe	400	N/A	N/A	7 Mar 2018
129	Pol Indp	400	0	Foil	7 Mar 2018
130	Pol Indp	400	0	Foil	7 Mar 2018
131	Pol Indp	400	45	Foil	7 Mar 2018
132	Pol Indp	400	45	Foil	7 Mar 2018
133	Long CO	400	0	Foil	7 Mar 2018
134	Long CO	400	0	Foil	7 Mar 2018
135	Long CO	400	90	Foil	7 Mar 2018
136	Long CO	400	90	Foil	7 Mar 2018
137	Long CO	400	90	Foil	7 Mar 2018
138	Long CO	400	45	Foil	7 Mar 2018
139	Long CO	400	45	Foil	7 Mar 2018

Table 3: Bend ratios for pipes with a given dimension ratio.

Dimension Ratio (DR)	Bend Ratio (α)
7	20
9	20
11	25
13.5	25
17	27
21	27

Table 4: Short term bend ratios for pipes with a given dimension ratio.

Dimension Ratio (DR)	Short-Term Bend Ratio (α_{st})
7.3	10
9	10
11	13
13.5	13
17	17
21	16

Table 5: Strains calculated for standard pipes at the minimum bend ratio for a variety of dimension ratios.

Size	OD	DR7			DR9			DR11			DR13.5			DR17	
3/4”	1.05	bend ratio wall 0.15 strain	20 bend radius 21 0.003332	y/D 0.00765	bend ratio wall 0.117 strain	20 bend radius 21 0.00431	y/D 0.01258	bend ratio wall 0.095 strain	25 bend radius 26.25 0.00339	y/D 0.01221	bend ratio wall strain	25 bend radius	y/D	bend ratio wall strain	be
1”	1.315	bend ratio wall 0.188 strain	20 bend radius 26.3 0.003329	y/D 0.007644	bend ratio wall 0.146 strain	20 bend radius 26.3 0.004331	y/D 0.01267	bend ratio wall 0.12 strain	25 bend radius 32.875 0.00336	y/D 0.01200	bend ratio wall strain	25 bend radius	y/D	bend ratio wall strain	be
1.25”	1.66	bend ratio wall 0.237 strain	20 bend radius 33.2 0.003334	y/D 0.007665	bend ratio wall 0.184 strain	20 bend radius 33.2 0.00433	y/D 0.01271	bend ratio wall 0.151 strain	25 bend radius 41.5 0.00337	y/D 0.01208	bend ratio wall strain	25 bend radius	y/D	bend ratio wall strain	be
1.5”	1.9	bend ratio wall 0.271 strain	20 bend radius 38 0.0033	y/D 0.007680	bend ratio wall 0.211 strain	20 bend radius 38 0.004330	y/D 0.012669	bend ratio wall 0.173 strain	25 bend radius 47.5 0.00337	y/D 0.01206	bend ratio wall strain	25 bend radius	y/D	bend ratio wall strain	be
2”	2.375	bend ratio wall 0.339 strain	20 bend radius 47.5 0.00333	y/D 0.007669	bend ratio wall 0.264 strain	20 bend radius 47.5 0.00432	y/D 0.01264	bend ratio wall 0.216 strain	25 bend radius 59.375 0.003380	y/D 0.01208	bend ratio wall 0.176 strain	25 bend radius 59.375 0.00420	y/D 0.01820	bend ratio wall 0.14 strain	be (
3”	3.5	bend ratio wall 0.5 strain	20 bend radius 70 0.003332	y/D 0.00765	bend ratio wall 0.389 strain	20 bend radius 70 0.00432	y/D 0.01264	bend ratio wall 0.318 strain	25 bend radius 87.5 0.00338	y/D 0.01211	bend ratio wall 0.259 strain	25 bend radius 87.5 0.004207	y/D 0.01826	bend ratio wall 0.206 strain	be 0
4”	4.5	bend ratio wall 0.643 strain	20 bend radius 90 0.003331	y/D 0.007652	bend ratio wall 0.5 strain	20 bend radius 90 0.00432	y/D 0.01265	bend ratio wall 0.409 strain	25 bend radius 112.5 0.00338	y/D 0.01210	bend ratio wall 0.333 strain	25 bend radius 112.5 0.004207	y/D 0.0182	bend ratio wall 0.265 strain	be (
5”	5.375	bend ratio wall 0.768 strain	20 bend radius 107.5 0.00333	y/D 0.007653	bend ratio wall 0.597 strain	20 bend radius 107.5 0.004330	y/D 0.01266	bend ratio wall 0.489 strain	25 bend radius 134.375 0.00337	y/D 0.01208	bend ratio wall 0.398 strain	25 bend radius 134.375 0.00420	y/D 0.01823	bend ratio wall 0.316 strain	be (
6”	6.625	bend ratio wall 0.946 strain	20 bend radius 132.5 0.00333	y/D 0.007663	bend ratio wall 0.908 strain	20 bend radius 132.5 0.00347	y/D 0.00831	bend ratio wall 0.736 strain	25 bend radius 165.625 0.00274	y/D 0.00810	bend ratio wall 0.602 strain	25 bend radius 165.625 0.00338	y/D 0.01211	bend ratio wall 0.491 strain	be (

.1 Single Material Tensile Tests

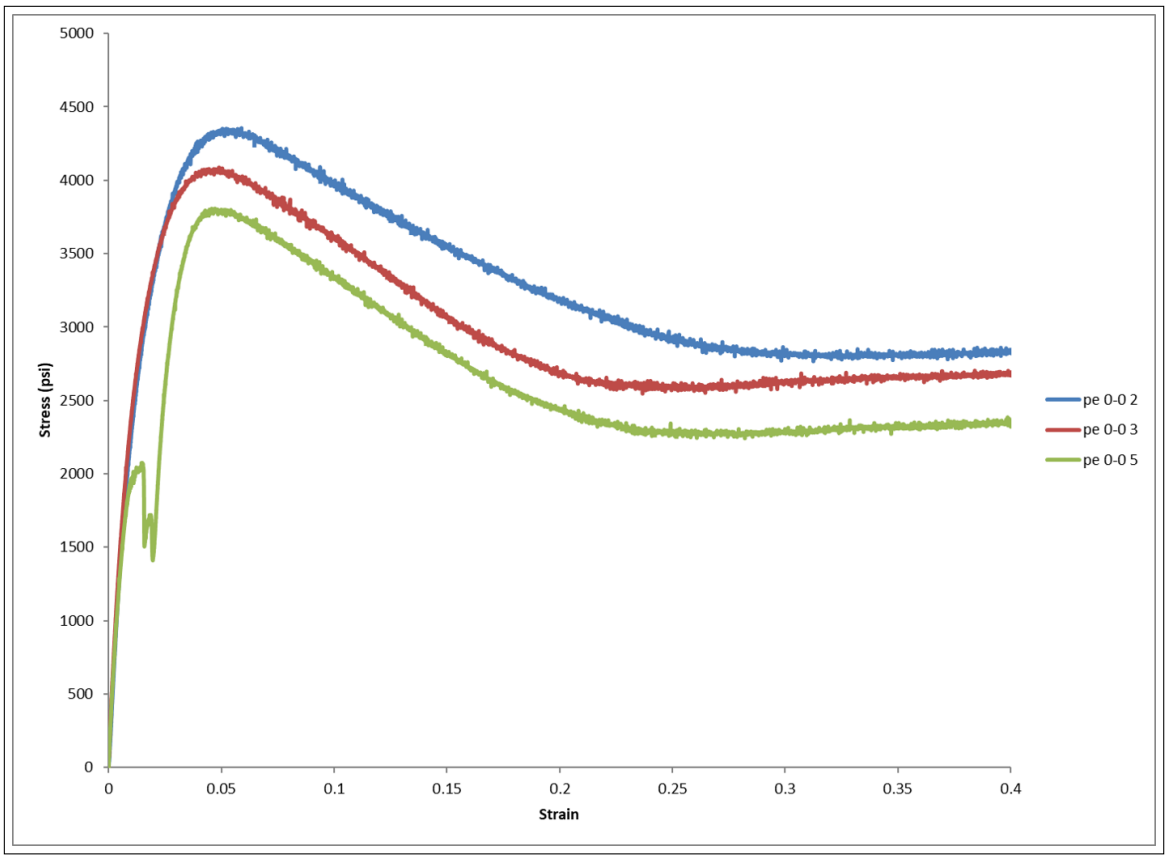

Figure 1: Stress vs. strain for neat polyethylene specimens.

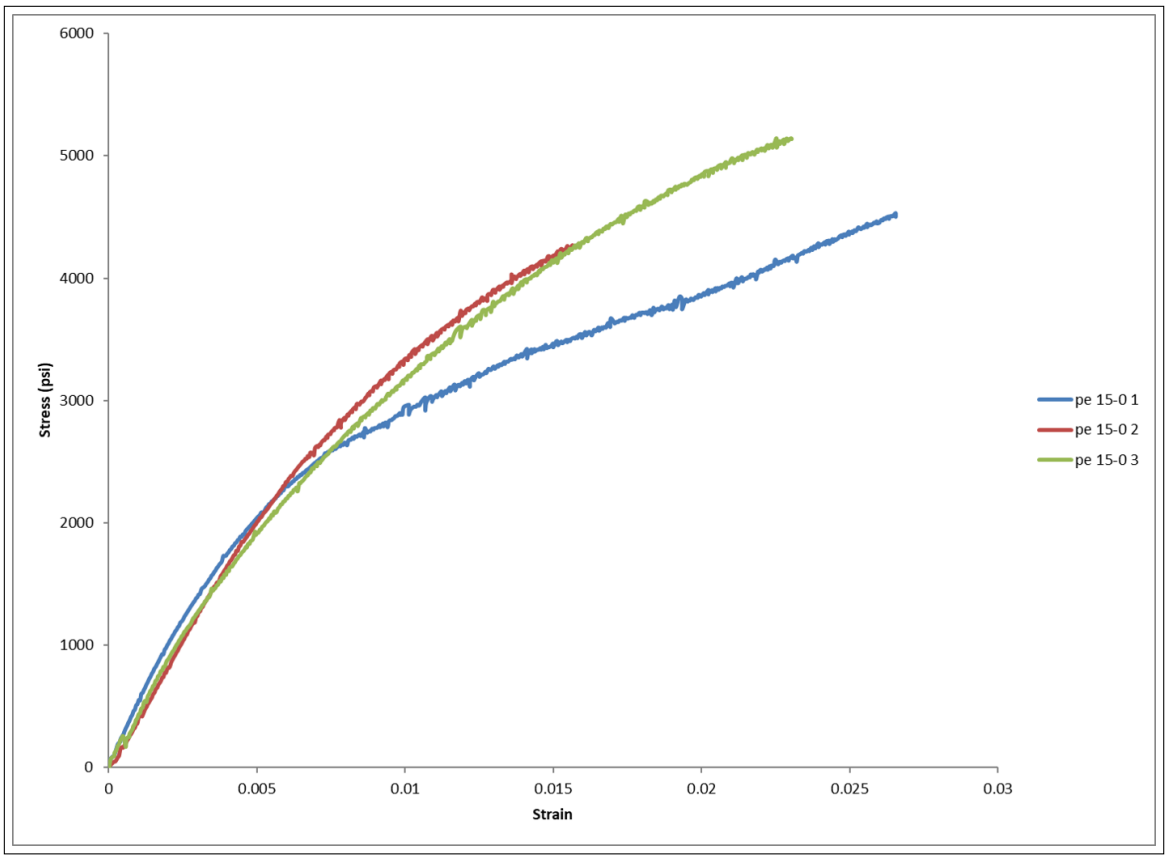

Figure 2: Stress vs. strain for polyethylene specimens with 15% carbon black.

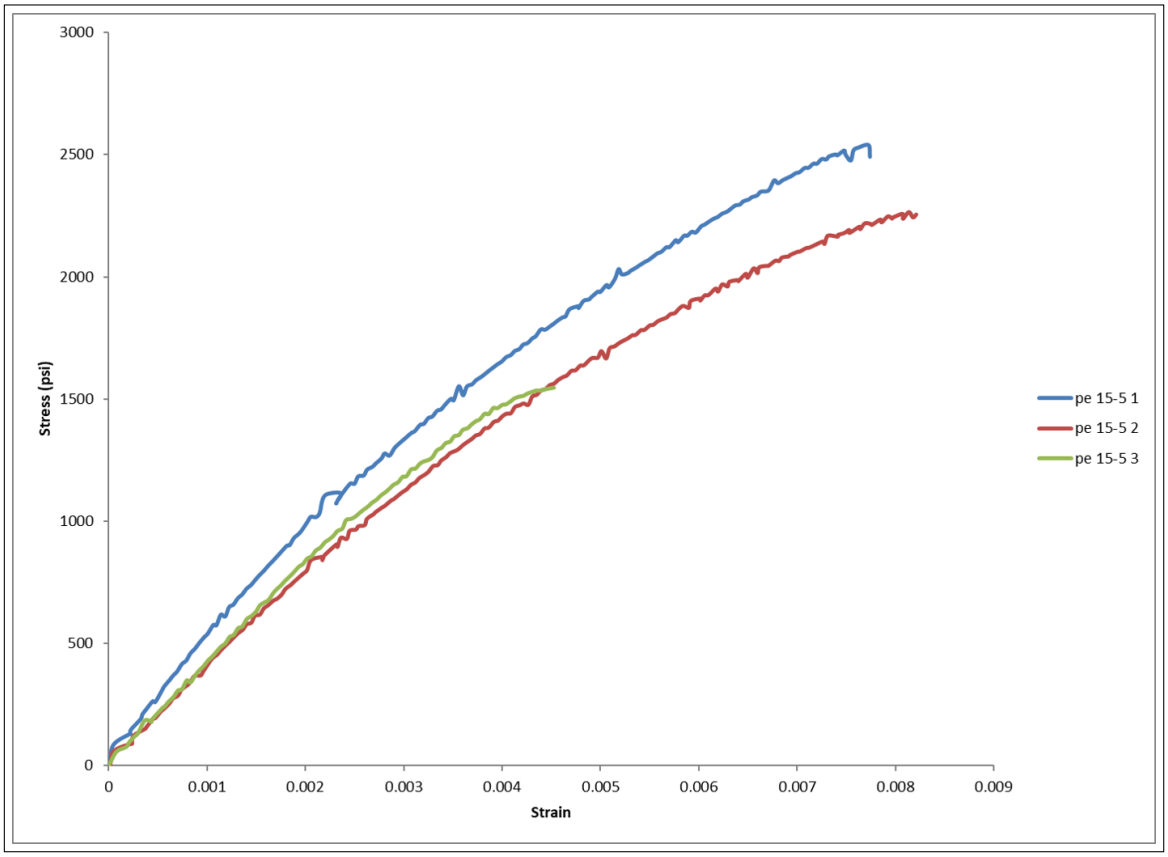

Figure 3: Stress vs. strain for polyethylene specimens with 15% carbon black and 5% aluminum flake.

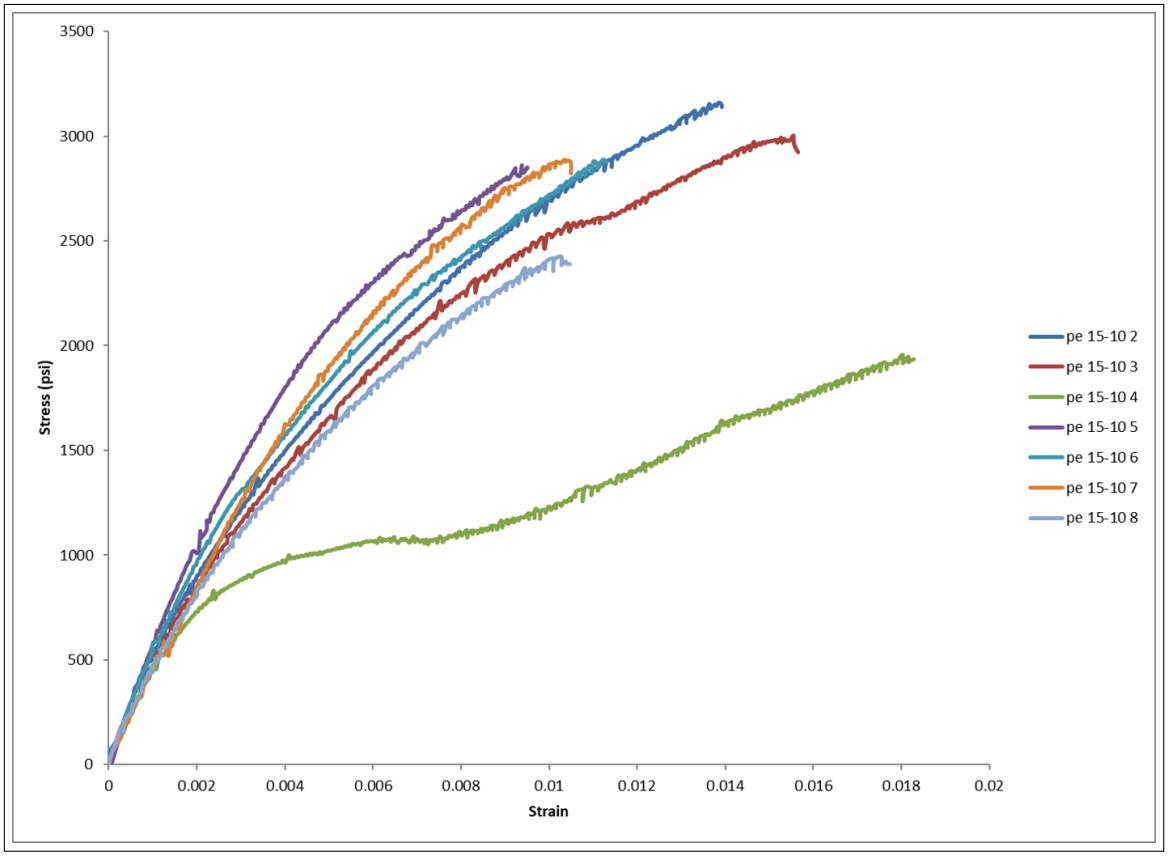

Figure 4: Stress vs. strain for polyethylene specimens with 15% carbon black and 10% aluminum flake.

.2 Bilayer Tensile Tests

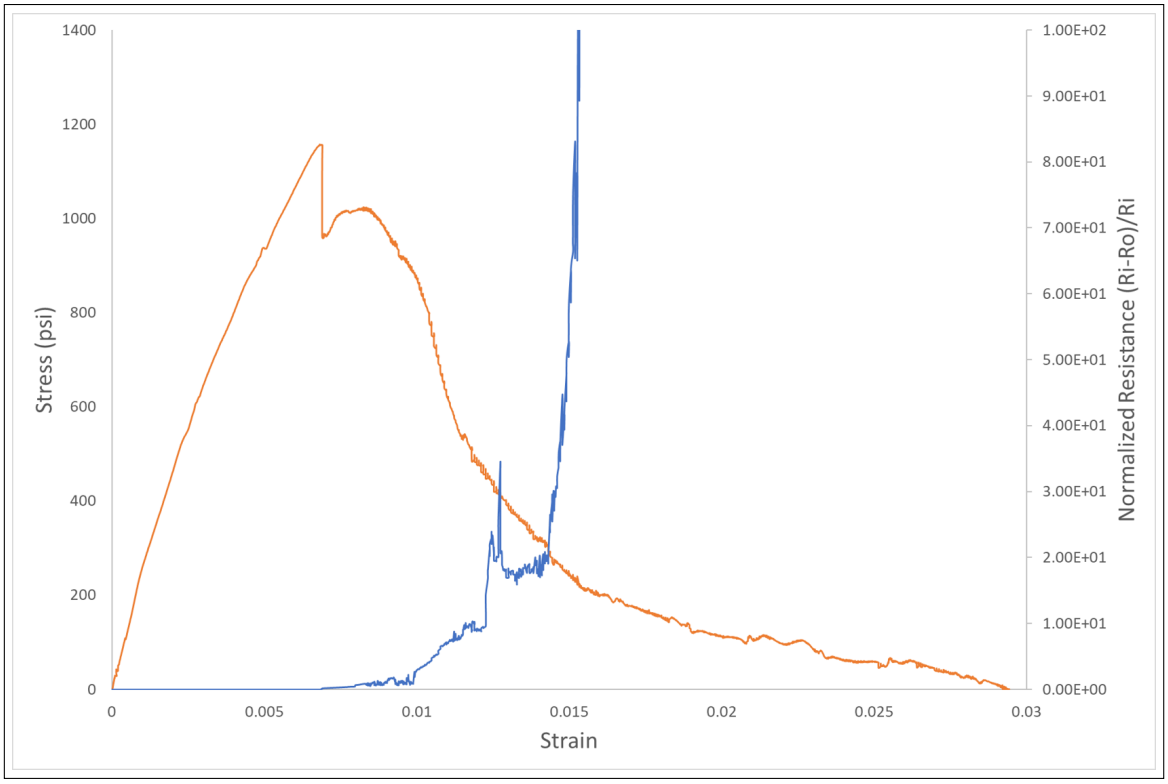

Figure 5: Stress vs. strain and normalized resistance vs strain for a polyethylene specimen with layers of doped and neat polyethylene.

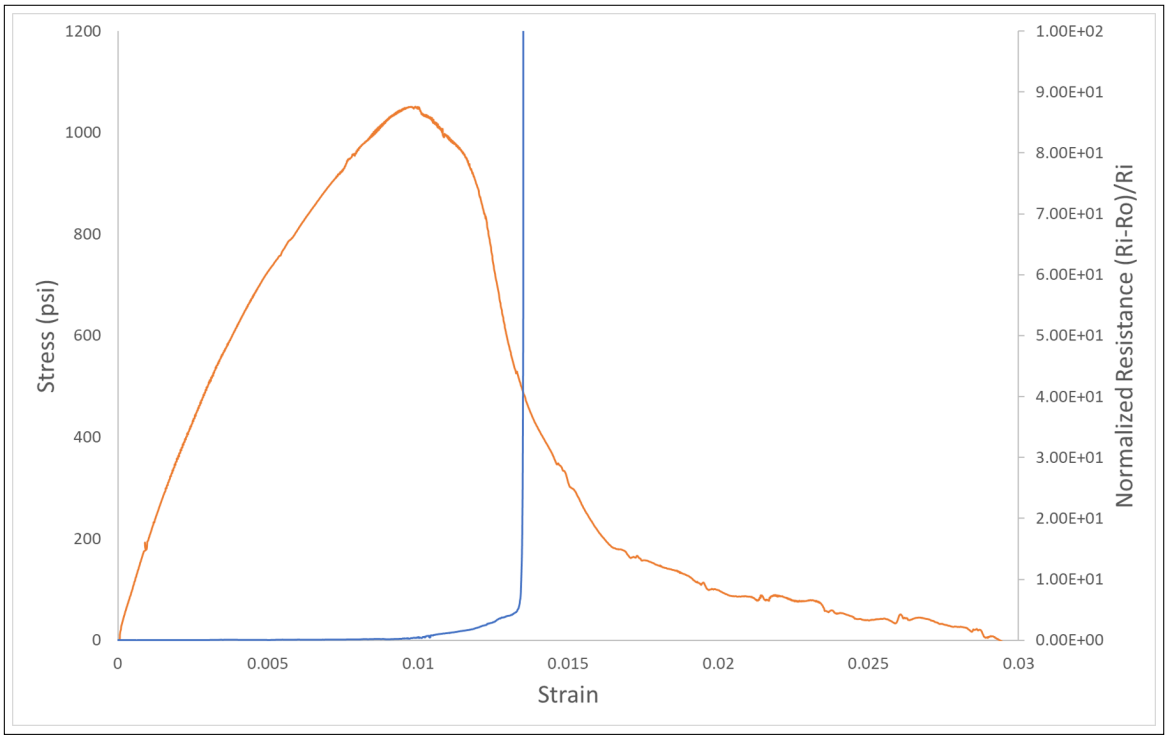

Figure 6: Stress vs. strain and normalized resistance vs strain for a polyethylene specimen with layers of doped and neat polyethylene.

.1 Single Material Tensile Tests

Figure 7: Cross section of a doped polyethylene tensile specimen.

Figure 8: Cross section of a doped polyethylene tensile specimen.

Figure 9: Cross section of a doped polyethylene tensile specimen.

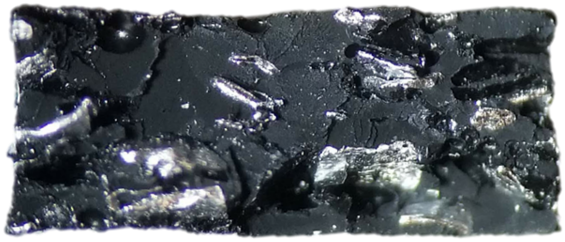

Figure 10: Cross section of a doped polyethylene tensile specimen.

Figure 11: Cross section of a doped polyethylene tensile specimen.

Figure 12: Cross section of a doped polyethylene tensile specimen.

.2 Bilayer Tensile Tests

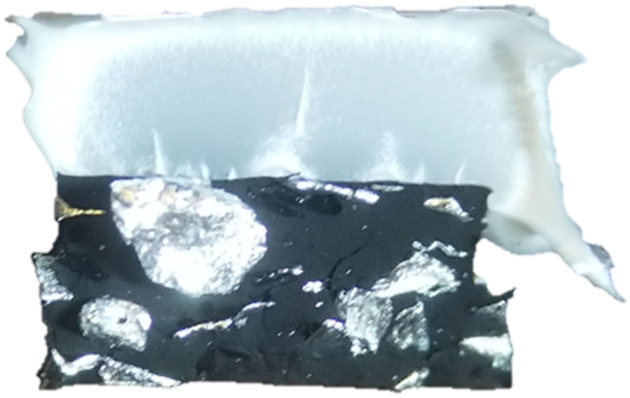

Figure 13: Fracture surface of a bilayer tensile specimen with doped and neat polyethylene layers.

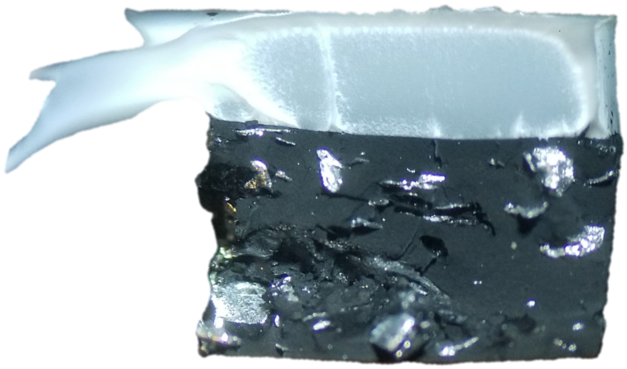

Figure 14: Fracture surface of a bilayer tensile specimen with doped and neat polyethylene layers.

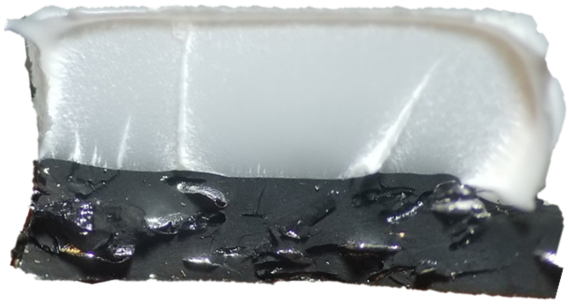

Figure 15: Fracture surface of a bilayer tensile specimen with doped and neat polyethylene layers.

Microcapsule Diameters

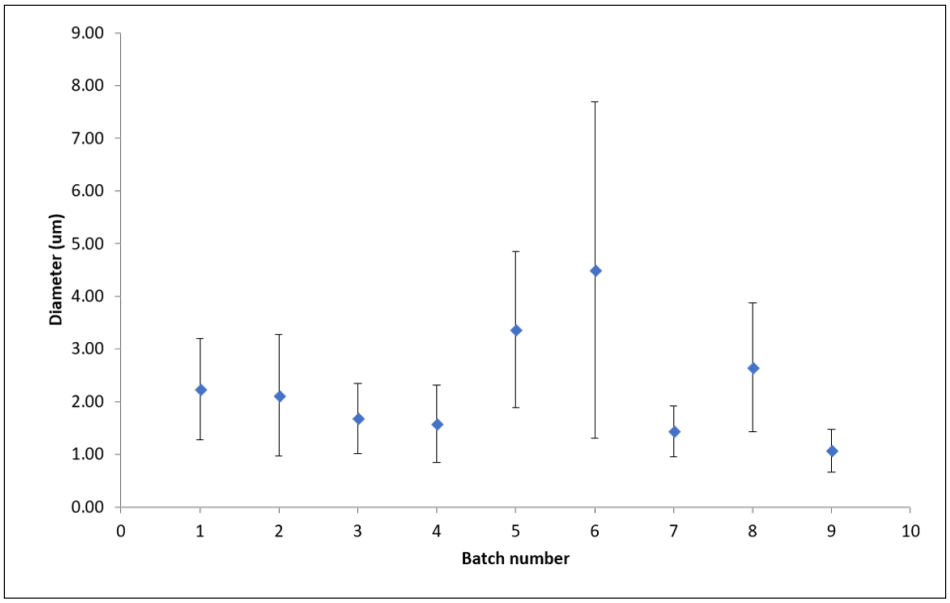

Figure 16: Average size and size distribution for all batches of capsules

Table 6: Legend for Figure 16.

Batch Number	1	2	3	4	5	6	7	8	9
Ultrahydrophobe Amount	0%	5%	5%	5%	5%	5%	5%	5%	5%
Mixer Speed	500	500	500	500	500	1000	200	500	200
Homogenizer Speed	3	3	3	1	3	3	3	5	1
Homogenizer time (minutes)	10	10	20	10	5	10	10	10	20

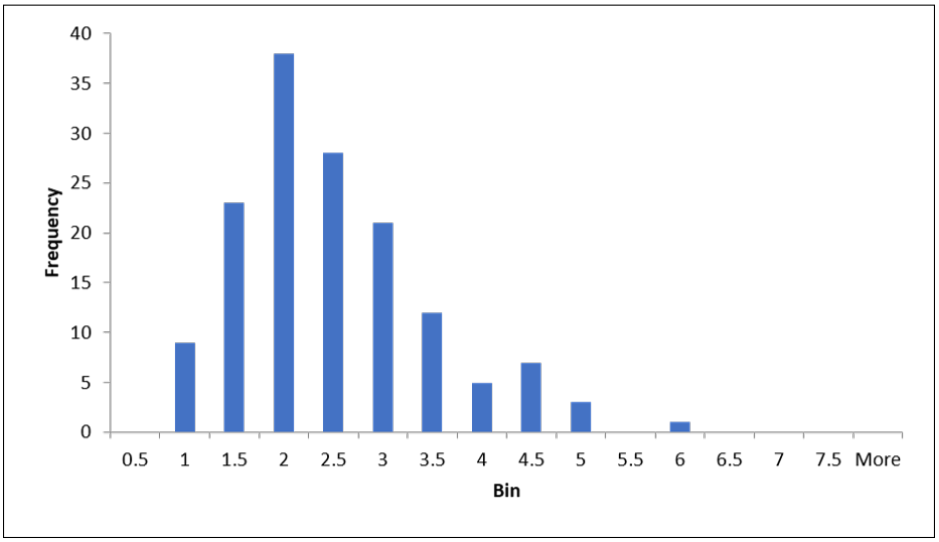

Figure 17: Urea formaldehyde microcapsules with no dodecane, mixed at 500 rpm with homogenizer at level 3 for 10 minutes.

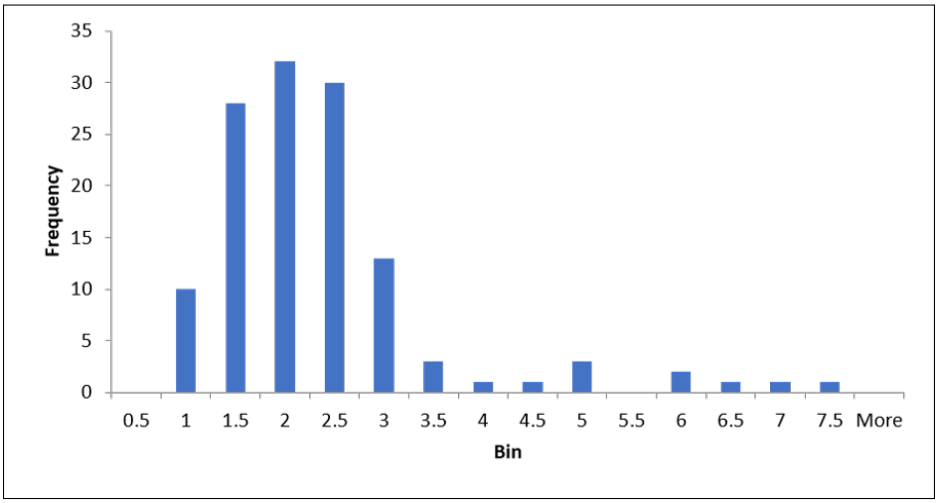

Figure 18: Urea formaldehyde microcapsules with 5% dodecane, mixed at 500 rpm with homogenizer at level 3 for 10 minutes.

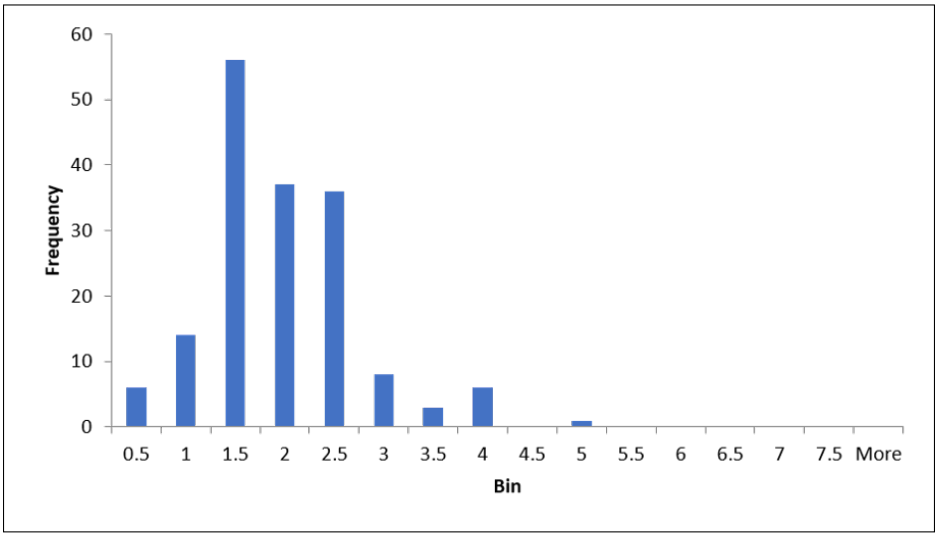

Figure 19: Urea formaldehyde microcapsules with 5% dodecane, mixed at 500 rpm with homogenizer at level 3 for 20 minutes.

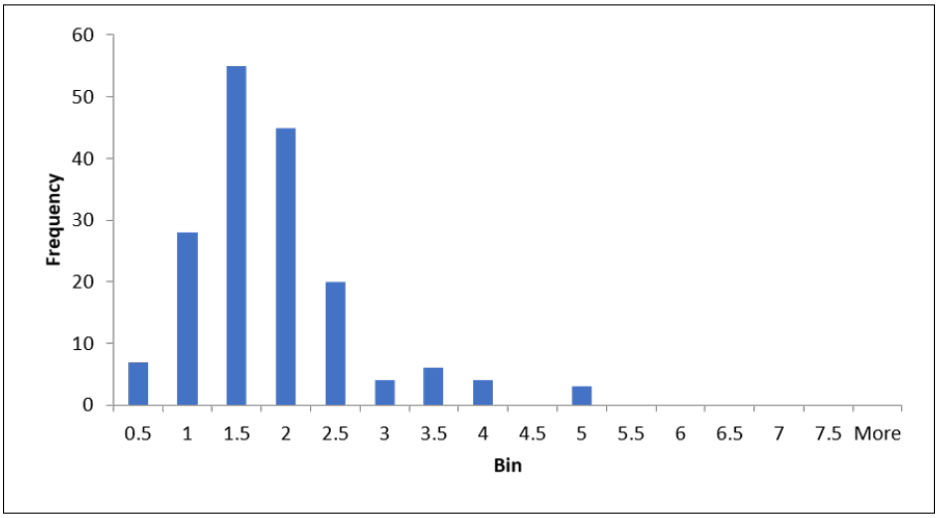

Figure 20: Urea formaldehyde microcapsules with 5% dodecane, mixed at 500 rpm with homogenizer at level 1 for 10 minutes.

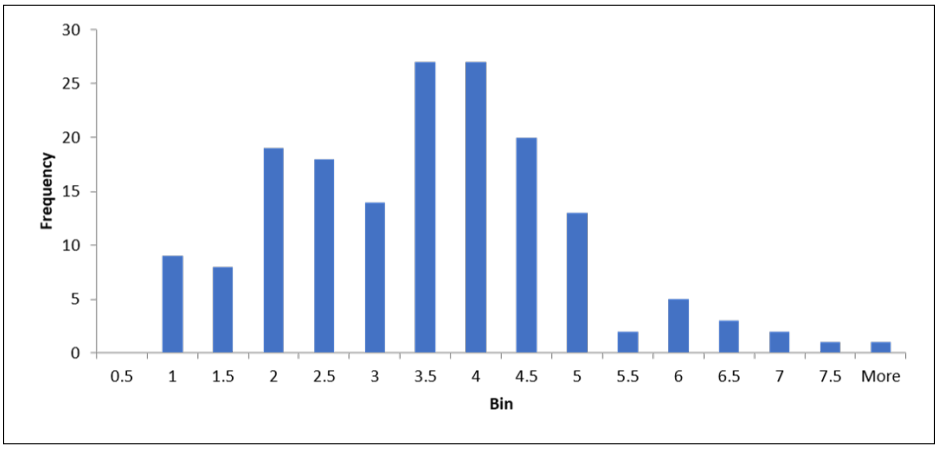

Figure 21: Urea formaldehyde microcapsules with 5% dodecane, mixed at 500 rpm with homogenizer at level 3 for 5 minutes.

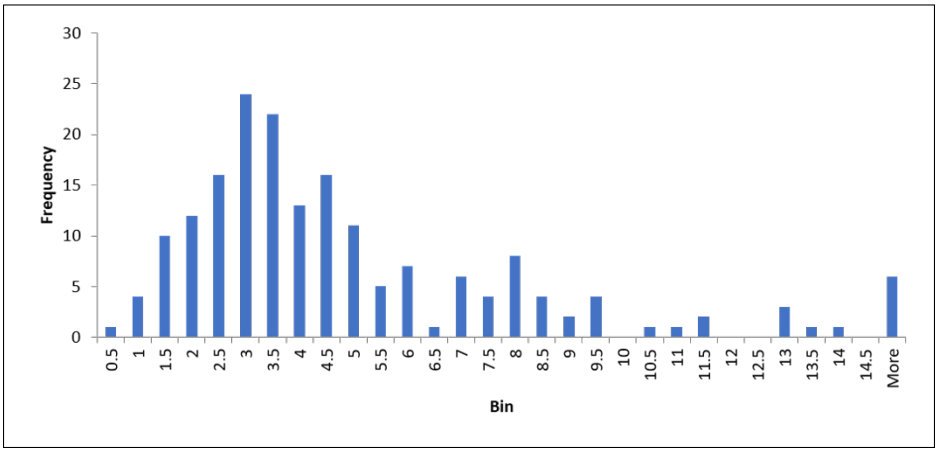

Figure 22: Urea formaldehyde microcapsules with 5% dodecane, mixed at 1000 rpm with homogenizer at level 3 for 10 minutes.

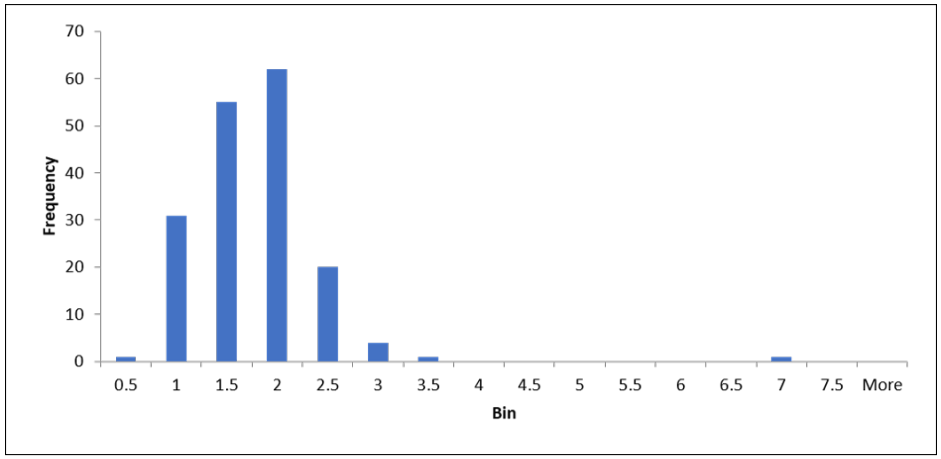

Figure 23: Urea formaldehyde microcapsules with 5% dodecane, mixed at 200 rpm with homogenizer at level 3 for 10 minutes.

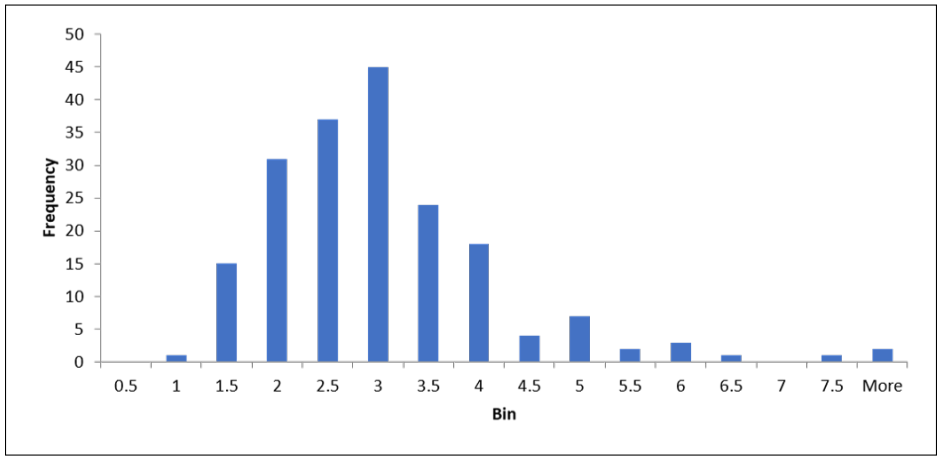

Figure 24: Urea formaldehyde microcapsules with 5% dodecane, mixed at 500 rpm with homogenizer at level 5 for 10 minutes.

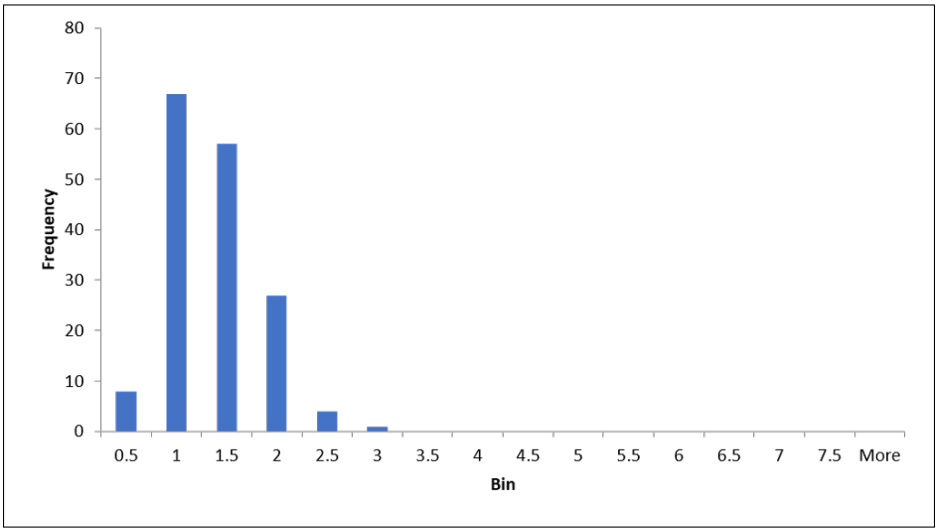

Figure 25: Urea formaldehyde microcapsules with 5% dodecane, mixed at 500 rpm with homogenizer at level 1 for 20 minutes.